Highlights

- Examine PBLH estimate with different platform/methods in NYC urban and coastal area;
- Compare diurnal variation of PBLH and O_3 in the urban and coastal area;
- Indicate O_3-rich plume in the coastal area due to urban transport, sea breezes and low PBL;
- Identify a model forecast bias on the

1   **Ozone pollution episodes and PBL height variation in the NYC urban and**
2   **coastal areas during LISTOS 2019**

3   Yonghua Wu [1, 2*], Kaihui Zhao [3], Xinrong Ren [4, 5], Russell R. Dickerson [5], Jianping Huang [6], Margaret J.
4   Schwab [7], Phillip R. Stratton [5], Hannah Daley [5], Dingdong Li [1], Fred Moshary [1, 2]

5   [1] Optical Remote Sensing Lab, City College of New York (CCNY), New York, NY 10031, USA,
6   [*] Email: yhwu@ccny.cuny.edu
7   [2] NOAA–Cooperative Science Center for Earth System Sciences and Remote Sensing Technologies
8   (CESSRST), NY 10031, USA
9   [3] Yunnan Key Laboratory of Meteorological Disasters and Climate Resources in the Greater Mekong
10   Sub-region, Yunnan University, Kunming, 650091, China
11 [4] Air Resources Laboratory, National Oceanic and Atmospheric Administration (NOAA), College Park
12   20742, MD, USA
13 [5] Department of Atmospheric and Oceanic Science, University of Maryland, College Park (UMD), MD
14   20742, USA
15 [6] NOAA/NCEP/ Environmental Modeling Center and Lynker, College Park, MD 20740, USA
16 [7] Atmospheric Sciences Research Center, University at Albany, State University of New York, Albany,
17   NY, USA
18

19 **Abstract** In summer, frequent ozone (O_3) episodes occur in New York City (NYC) and coastal areas along
20 Long Island Sound (LIS) due to complex interplay of urban pollutants transport, land-sea breezes, and
21 chemistry. The Long Island Sound Tropospheric Ozone Study (LISTOS) was carried out to address this
22 issue; here we present an integrated analysis of the diurnal variation of planetary-boundary-layer height
23 (PBLH) and O_3 in the NYC urban and coastal area during LISTOS in summer 2019. A persistent O_3 episode
24 (July 28-31, 2019) is investigated which shows much higher O_3 (90-120 ppb with 5-min average maximum)
25 along the North-shore of Long Island (NLI) than the NYC urban and South-shore of Long Island (SLI). We
26 evaluate the PBLH estimate with a multi-platform observation in the complex coastal environment, and
27 compare the PBLH diurnal variation in the NYC urban to coastal areas. The results indicate lower PBLH
28 in the mid-morning and noon in the NLI than the NYC urban area. With the simultaneously measured O_3
29 and PBLH, the integrated O_3 content or total content in the PBL defined as the O_3 concentrations
30 multiplying PBLH show good consistency in the urban and NLI coast at noon on July 28-29, 2019. A dense
31 O_3 plume, rich in CO, aerosols, black carbon, HCHO and NOx appeared in the PBL as detected from the
32 UMD Cessna research aircraft, satellite TROPOMI and ozonesonde; their coincidently large values imply
33 the combined impacts of urban plumes transport, lower PBLH and land-sea breezes in the NLI area. Finally,
34 we evaluated the forecast of O_3 and PBLH from the NOAA NAM-CMAQ (12 km grid) and WRF-Chem
35 (1.3 km grid) models with the observations. Both models show good agreement with the observations at
36 the NYC urban site; but at the NLI coastal site, the NAM-CMAQ model forecast indicates a timing bias for
37 the maximum O_3 at noon. These results provide insight into the impacts of the sea breeze and urban heat
38 island on air quality.

39 **Keywords**: Ozone, PBL, Transport, Sea breezes

40 **1. Introduction**

Ozone (O_3) exceedances of National Ambient Air Quality Standard (NAAQS, 70 ppb daily maximum 8-hour average ozone, DM8AO) frequently occur during summer in New York City (NYC) and its downwind coastal areas in Long Island and Connecticut or Long Island Sound (Miller, 2017; Karambelas, 2020). Such high O_3 episodes are generally related to complex interaction of urban emissions and pollutants, photochemical transformation, transport, and land-sea breezes effects (Karambelas, 2020). To understand high O_3 formation processes, the Long Island Sound Tropospheric Ozone Study (LISTOS) campaign was launched in summer 2018 and 2019 (https://www.nescaum.org/documents/listos). The measurements were made from the land sites, research aircrafts and marine vessels, and space in Long Island Sound (LIS) where a land–sea breeze feature can lead to high O_3 concentrations along the shoreline of Connecticut and New York State (see more logistic information in Karambelas, 2020).

Planetary boundary layer height (PBLH), dynamics and structure often affect the pollutants dispersion and transport. Angevine et al. (2004) indicate the coastal boundary layer influence on pollutant transport in New England during the New England Air Quality Study (NEAQS). The lack of vertical mixing and deposition over the water and the sea breezes could affect the air pollutant transport levels in the coastal area over the Galveston Bay in Houston area (Angevine et al., 2008). The shallow PBLH can keep the morning emissions and pollutants confined at near-surface. In addition, the land-water breezes have been investigated to understand O_3 accumulation in the coastal areas (Caicedo et al., 2019 and 2021; Day et al., 2010; Finardi et al., 2018; Goldberg et al., 2014; Han et al., 2022; Loughner et al., 2011, 2014; Stuffer et al., 2015; Vermeuel, et al., 2019; Zhang et al., 2020). Zhang et al (2020) show a sharp gradient of O_3 at and near the land-water interface in Long Island using a mobile measurement during LISTOS 2018, which is attributed to the sea-breezes in the Northern Long Island. Han et al. (2022) analyzed sea breezes life cycle in and around NYC that made dramatic impacts ozone patterns in NYC region. Caicedo et al. (2019 and 2021) showed that the different bay-breezes in the horizontal and vertical evolution of wind affected the O_3 vertical structure during the Ozone Water-Land Environmental Transition Study Phase-2 (OWLETS-2) campaign (Sullivan et al., 2019). On the other hand, Tao et al. (2022) compared the PBLH on five O_3 exceedances and five nonexceedance days during the LISTOS campaign in NYC using the WRF-CMAQ simulation product (1.33 km grid resolution), and the results indicated lower PBLH on O_3-exceedance days at noon time with a regional mean decrease of 0.22-0.24 km.

According to Stull (2012), a convective boundary layer (CBL) that occurs in the daytime is usually referred to as a mixing layer (ML); under this situation, the mixing layer height (MLH) is equivalent to PBLH (the MLH and PBLH may be used in the content of this paper). Ceilometer and Coherent Doppler Wind lidar are extensively deployed to make continuous observation of PBLH or MLH and dynamics (Caicedo et al., 2020, Haeffelin et al., 2012, Schween et al., 2014, Tucker et al., 2009, Zhang et al., 2022). The MLH can be estimated from the ceilometer-measured aerosol profile through locating sharp gradient of attenuated backscatter distribution. However, large uncertainty stems from aloft aerosol layers, residual aerosols and low-level clouds, thus a quality control and quality assurance (QA/QC) process is often required to remove those outliers for the MLH estimate (Caicedo et al., 2020, Haeffelin et al., 2012; Li et al., 2022). Particularly for transported urban and wildfire smoke plume to the coastal area, the gradient at the aloft-layer top may not represent local MLH. On the other hand, Coherent Doppler Wind Lidar (CDWL) is widely used to measure the 3D winds in the PBL. Most commercial CDWL is operated at around 1.5 µm wavelength and its signal-to-noises (SNR) or carrier-to-noise ratios (CNR) depend on aerosol concentrations. Vertical motions in the PBL can be quantified from vertical stares (non-scanning mode)

83 performed by a Doppler wind lidar, and variance of vertical velocity generally represents vertical mixing
84 or turbulence intensity thereby indicating convective boundary layer height (CBLH) or MLH (Tucker et al.,
85 2009). However, this method requires an empirical threshold for the MLH estimate and this threshold may
86 vary with the vertical turbulent intensity and geo-location, and it may not work properly under stable
87 boundary layer (SBL) condition due to weak turbulence, particularly over the water and coastal area
88 (Schween et al., 2014, Tucker et al., 2009). Alternatively, a gradient method for CNR profile is used for the
89 SBL height (SBLH) estimate but suffers similar issue as the ceilometer method due to aloft aerosol layer
90 and low CNR issues. On the other hand, a gradient method on the horizontal wind profile may work for the
91 SBLH estimate (Tucker et al., 2009). Another issue is that the ceilometer and wind lidar generally collect
92 reliable atmospheric returns above 100-m altitude; thus shallow SBLH lower than 100-m is difficult to
93 detect from their measurements. In the meantime, meteorology-based methods (e.g., potential temperature
94 gradient or Richardson number (R_i)) from radiosonde measurements can also be used to determine the
95 PBLH though such observations are routinely made twice per day (00:00 and 12:00 UTC) at national
96 weather station. Thus, it is important to evaluate PBLH or MLH estimate among these different methods in
97 the coastal area while the LISTOS campaign provides an opportunity for this research purpose.
98   In addition, air quality models such as the Community Multiscale Air Quality modeling (CMAQ) have
99 been extensively used to predict O_3 and address high O_3 events (Dreessen et al., 2016), but there are
100 potentially large uncertainties in coastal areas due to complex meteorological effects over the land-water
101 interface and limited spatial resolution (Abdi-Oskouei et al., 2020; Ma et al., 2021; Torres-Vazquez1 et al.,
102 2022; Bernier et al., 2022). For instance, using the WRF-Chem (4 km horizontal or grid resolution) over
103 the Lake Michigan Ozone Study 2017 (LMOS), Abdi-Oskouei et al. (2020) indicated that the model skill
104 on Lake breeze was inconsistent depending on site and day; for some sites or cases, hourly peak O_3 from
105 WRF-Chem could be underestimated and the bias might be attributed to transport and lake breeze errors.
106 They also found that increases in hydrocarbon emissions could increase O_3 production by the model and
107 reduce the mode error over the Lake Michigan. Previous studies (Loughner et al., 2011, 2014; Goldberg et
108 al., 2014; Caicedo et al., 2019) indicate that the timing and strength of the sea-breeze are key for correctly
109 simulating pollution events whereas it is a challenge to model simulation of sea-breezes as they are sensitive
110 to the land-water surface contrast, spatially coarse initial conditions and horizontal resolution. It was found
111 that the initial analysis and land surface behavior for the WRF modeling were the important items in getting
112 good simulations of PBLH and O_3 (Angevine et al., 2008). In addition, Torres-Vazquez1 (2022) evaluated
113 the WRF-CMAQ simulation performance of the meteorology and O_3 for the LISTOS 2018, and the two
114 cases studies suggest that higher spatial resolution (1.3 km grid) improve surface meteorology simulation
115 throughout the whole summer; and the sound breezes and low-level jets played an important role in the
116 transport of urban emissions and pollutants to marine boundary layer in LIS and advection to the CT coast.
117 In addition, in the NYC urban area anthropogenic volatile chemical products (VCPs) and volatile organic
118 compounds (VOCs) can make a great contribution to high O_3 production (Coggan et al., 2021; Ring et al.,
119 2023), thus becoming important for the models to achieve accurate predictions.
120   Synergistic and collaborative measurements and model studies have been performed in LISTOS
121 campaigns for understanding high O_3 formation and transport mechanisms. One of the major concerns is
122 how the urban plume transport, PBL dynamics, and land-sea breeze affect near-surface O_3 during the O_3
123 episodes period in the coastal area. The scopes of this study include: 1) evaluating PBLH estimate among
124 the different methods/instruments, and comparing the PBLH dynamics in the NYC urban and coastal area;

125   2) analyzing high O_3 formation relevant to vertical mixing, PBLH, sea breezes and urban plume transport
126   in the coastal area; 3) assessing the model forecast of O_3 and PBLH by the NOAA NAM-CMAQ and WRF-
127   Chem at the NYC urban and coastal sites. This paper is organized as follows, Section-2 gives the
128   observation and methodology; Section-3 presents the results and discussions, with the conclusions
129   following in Section 4.
130

2. Observation and Methodology

2.1 Ground-based observations

133   At the City College of New York (CCNY) site (40.820° N, 73.949° W), there are a suite of remote sensing
134   and in-situ instruments for air quality and meteorological observations, which include a ceilometer, a 3-
135   wavelength elastic-Raman scattering lidar, a microwave radiometer (Radiometric MP-3000A), a Cimel
136   sun/sky radiometer in part of AERONET (Aerosol Robotic Network), a coherent Doppler wind lidar
137   (Leosphere Windcube 200S), in-situ samplers for O_3, NO_2 and aerosol size distribution and a weather
138   station. The observations are mostly operated with 1-min average. Meanwhile, a surface air quality
139   monitoring station (AQS) is operated by New York State Department of Environmental Conservation
140   (NYSDEC) at CCNY campus for O_3, CO and $PM_{2.5}$ measurement. **Figure 1** and Table-1 show the
141   geolocations of CCNY-site and other ground sites used in this study.
142   At CCNY, a Lufft ceilometer (CHM15K) measures aerosol backscatter at a laser wavelength of 1064
143   nm with a vertical range resolution of 15-m and time resolution of 15-second. It makes fully automatic 24-
144   hr/7-day observations under all-weather conditions and provides attenuated backscatter coefficient profiles
145   that can be used to determine aerosol layer height (ALH) and cloud base height (CBH). The valid return
146   signals start from around 150~180 m altitude due to inherent geometric overlap function between the
147   transmitter and receiver (Li et al., 2021). In this study, we use a wavelet transform method to determine
148   the PBLH, and a quality control algorithm is performed which includes cloud screening, temporal
149   continuity, and screening of an aloft or residual layer during the night and early-morning (Gan et al., 2011,
150   Li et al., 2022). A residual-layer-height (RLH) can be estimated from the second sharp gradient of aerosol
151   profile in the early morning. In addition, the CCNY elastic-Raman lidar transmits three wavelengths (1064-,
152   532- and 355-nm) with a flash lamp-pumped Nd: YAG laser at a repetition rate of 30 Hz (Spectra-physics
153   Quanta-Ray PRO-320) (Wu et al., 2009). A receiver telescope (Ø50-cm) collects three elastic scattering
154   and two Raman-scattering returns by nitrogen and water vapor molecules excited by the 355-nm laser
155   output. It is generally operated during daytime on weekdays with an observer due to eye-safety concerns in
156   the NYC urban area. The strong signal-to-noise ratios (SNR) of this lidar allow us to measure aloft aerosol
157   plumes and retrieve aerosol extinction and backscatter profile; thus one can obtain PBLH and aloft aerosol
158   plumes optical properties (Gan et al., 2011, Wu et al., 2012, 2019 and 2021).
159   In addition, two sets of ceilometers (Vaisala CL51 and CL31) and O_3 monitors (2B Tech model
160   202/205) are deployed at the North-shore (Eatons Neck, 40.954176°N, 73.398471°W) and South-shore
161   (Fire Island, 40.625282°N, 73.257897°W) of Long Island during July 22-Oct.15, 2019, respectively. These
162   two sites are close to the waterfront (a few tens meters distance). The attenuated backscatter profiles at the
163   wavelength of 905-nm are collected with a range resolution of 10-m and time resolution of 16-second. We
164   estimate the PBLH or MLH using a wavelet transform analysis and quality assurance method with a 10-
165   min average (Li et al., 2022). Meanwhile, near-surface O_3 data are collected with 5-min average. We
166   validated the O_3 data of the 2B-Tech monitors with the NYSDEC operated sampler before we deployed

167   them to the coastal sites; the data were simultaneously collected at the NYSDEC AQS at CCNY during
168   July 9-14, 2019, and the results indicate strong correlation with correlation coefficient R>0.99 and a linear
169   slope of 1.02~1.03 (See **Fig. S1(a)-(b) in Supporting Document**). We also validated our NO_2 data by
170   comparing them to the NYSDEC monitor data. The results indicate good correlation with R=0.995, linear
171   regression slope=1.07 and intercept value of 0.36 (**See Fig.S1(c)-(d) in Supporting Document)**. Therefore,
172   near-surface O_3, PBLH, low-altitude aerosol plumes and cloud height can be simultaneously measured in
173   the NYC urban (CCNY) and its downwind coastal area in Long Island (Eatons Neck and Fire Island). In
174   addition, a few other AQS for O_3 measurements are operated by NYSDEC at the coastal area, e.g., Flax
175   Pond (O_3, NO_2 and NO_y), Riverhead (O_3) at the North-Shore of Long Island (NLI), Babylon (O_3) near to
176   South Long Island (SLI). Further details about these sites can be found at the website
177   (http://www.dec.ny.gov/chemical/8406.html). Fig.1 and Table-1 give the site locations, coordinates and
178   data used in this study.
179   As part of the NYS-Mesonet (Brotzge et al., 2020, Shrestha et al., 2021), Coherent Doppler Wind
180   Lidars (Leosphere WindCube 100s) are deployed to measure wind profiles in Bronx (Lehman College,
181   40.87248° N, 73. 8935° W, 59.3 m ASL, 7.5 km away from CCNY, urban), Stony Brook (40.9196°N, -
182   73.1333°W, 55.1 m ASL) near the North-shore of Long Island, and Wantagh (40.6503°N, 73.5054°W,
183   18.25 m ASL) at the South-shore Long Island, respectively (See Fig.1 for their location). The wind lidar
184   emits the eye-safe laser beams at the wavelength 1.54 μm and a repetition rate of 10 kHz. It uses a vertically-
185   pointing beam to measure vertical wind velocity, and a Doppler Beam Swinging (DBS) scan mode
186   (elevation angle 75 degrees) to obtain horizontal wind velocity and direction. All data are collected, quality-
187   controlled, and archived (Brotzge et al., 2020, Shrestha et al., 2021). It provides 24-hr/7-day wind profile
188   measurements under all weather conditions. The constructional 3D-wind products have a range-gate
189   spacing of 25-50 m and a time resolution of 5~20 seconds. In this study, we estimate the PBLH or MLH
190   using the variance of vertical velocity with a threshold method (e.g., 0.1-0.15 m/s^2) during the convective
191   boundary layer (CBL) period (Tucker et al., 2019, Wu et al., 2019). Meanwhile, during the stable boundary
192   layer (SBL) period in the morning and night, the PBLH is calculated with the vertical gradient of horizontal
193   wind with a threshold (0.02-0.04 per second) (Tucker et al., 2019, Dai et al., 2014). The PBLHs from the
194   wind lidar and ceilometer estimates are evaluated with the meteorological profile-based method (e.g.,
195   potential temperature) measured by the radiosonde launched at a National Weather Service station at Upton
196   (OKX, 40.86° N, 72.86° W, 20-m ASL) and the ozonesonde at Flax Pond (40.9615° N, 73.13872° W).
197   The ozonesondes are launched at Stony Brook (SBK) during LISTOS 2019 and at the Flax Pond
198   Marine Laboratory (40.9615° N, 73.13872° W) during the LISTOS 2018 campaign (Couillard et al., 2021),
199   both sites are located near the North shore of Long Island. Vaisala radiosondes (Vaisala RS41-SGP) with
200   an En-Sci Electrochemical Cell ozonesonde (En-Sci) provided data at 1-sec intervals, with an uncertainty
201   of 5-10% on the ozone mixing ratio in the troposphere and ~5% in stratosphere (Witte et al., 2018). Vertical
202   profiles of O_3 and meteorological parameters (temperature, pressure, wind, relative humidity-RH) are
203   recorded. Nearby Flax Pond (surface O_3 site) and Stony Brook (wind-lidar and ozonesonde site in this
204   study), the radiosondes are routinely launched at OKX site twice per day (12:00 UTC and 24:00 UTC) for
205   profiling temperature, pressure, RH and winds. During the CBL period, the PBLH is determined from the
206   sharp increase of virtual potential temperature (Seidel et al., 2010; Dai et al., 2014). During the SBL period,
207   the PBLH is estimated from the inversion temperature height. The distance is about 22 km between the
208   radiosonde-OKX and wind-lidar site (SBK), 4.8 km between surface O_3 site (Flax Pond) and wind-lidar

209 site (SBK), 20-km between the ceilometer-site (Eatons Neck) and wind-lidar site (SBK), respectively.

210 Therefore, with the distances noted, we compare the PBLH bias among the wind lidar, ceilometer and

211 radiosonde measurements. All ground sites used in this study are shown in Fig.1 and Tab.1.
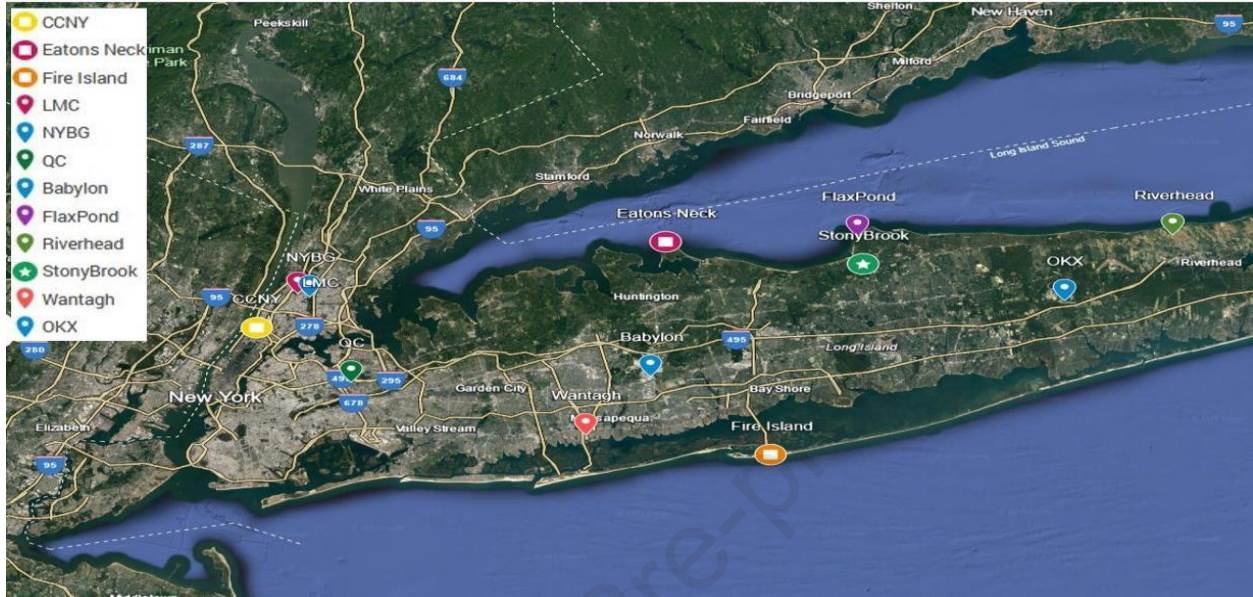
212

213

214 **Fig.1**. Ground sites used in this study (See Table-1 for their coordinates and observations).

215

216 **Table-1. Ground site location and the data used in this study***

Site-name	Latitude	Longitude	Data used		Operator, landmark
	(north, deg)	(west, deg)	Surface	Profile	
CCNY	40.821	-73.949	O_3, NO_2, T, Wind	Aerosol	CCNY+NYSDEC, Urban
Eatons Neck	40.954	-73.398	O_3	Aerosol	CCNY, Coast, NLI
Fire Island	40.625	-73.258	O_3	Aerosol	CCNY, Coast, SLI
NYBG	40.868	-73.878	O_3		NYSDEC-AQS, Urban
QC	40.736	-73.822	O_3, NO_2		NYSDEC-AQS, Urban
Babylon	40.745	-73.419	O_3		NYSDEC-AQS, Coast
Riverhead	40.961	-72.712	O_3		NYSDEC-AQS, Coast
Flax Pond	40.961	-73.138	O_3, NO_2		NYSDEC+ASRC, Coast
LMC(Bronx)	40.873	-73.894		Wind	NYS-Mesonet, Urban
Stony Brook	40.920	-73.133	T, Wind	Wind, O_3	NYS-Mesonet+ASRC
Wantagh	40.650	-73.505		Wind	NYS-Mesonet, Coast
OKX	40.860	-72.86		T, Wind	NOAA-NWS

217

218 *The acronyms in Table-1 are spelled with their full names in the contexts. See the site location in Fig.1. All

219 sites are continuously collected the data for 24 hours/7 days except OKX-site radiosonde launch twice per

220 day.

6

2.2 University of Maryland (UMD) research aircraft observations

The UMD Cessna research aircraft was deployed to measure gas compounds (O_3, CO, NOx, Formaldehyde *(*HCHO), CO_2, CH_4, etc.), aerosol optical properties (total scattering and absorption), black carbon (BC) and meteorological parameters during the LISTOS campaigns. This study uses the data measured in Long Island and NYC area on July 29, 2019. In particular, its simultaneous measurements of vertical profiles of aerosol, potential temperature, H_2O, and winds can be used to evaluate the PBLH estimate from the different methods; and its low-leg flight measurements can help assess spatial homogeneity of O_3 and other pollutants/parameters in the NYC and LIS region. The technical details on the instruments and observations can be found in the literatures (Taubman et al., 2004, Castellanos et al., 2011; Ren et al., 2018, 2019).

2.3 Satellite sensors for NO₂, HCHO and smoke plumes

TROPOspheric Monitoring Instrument (TROPOMI) on board the EPA Sentinel 5 Precursor (S5P) satellite was launched in October 2017 (Griffin, et al., 2019). It is a UV, visible (Vis), near-infrared, shortwave infrared backscattering sensor with an overpass time of 13:30 local solar time. Tropospheric column amounts of NO_2 and HCHO product from TROPOMI are used in this study. The Level-2 data have the spatial resolution of 7 km x 3.5 km (at nadir) during Apr.30, 2018 to Aug.6, 2019 and 3.5 km×5.5 km since Aug.6, 2019. The level-2 data product are downloaded (disc.gsfc.nasa.gov/) and selected with the quality assurance (QA>0.5).

NASA space-borne lidar CALIOP instrument on board the CALIPSO satellite platform observes global aerosol/cloud vertical distribution and provides aerosol type classification and optical properties products (Winker et al., 2009). It is a polarization-sensitive two-wavelength (532- and 1064-nm) lidar. In this study, the vertical distribution of Level-1 attenuated backscatters and the Level-2 aerosol subtypes product (Version 4.10) are used to identify aerosol plumes and their types around NYC area.

In addition, the NOAA Hazard Mapping System (HMS) was developed in 2001 by the National Environmental Satellite and Data Information Service (NESDIS) as an interactive tool to identify fires and smoke emissions over North America in an operational environment (Ruminski et al., 2006). The system utilizes two geostationary and five polar orbiting environmental satellites (https://www.ospo.noaa.gov/Products/land/hms.html). The result is a quality-controlled display of the locations of fires and significant smoke plumes. HMS has a number of detection limitations such as clouds hindering detections, no vertical structure information and no quantitative amount or density of smokes and is only available during daylight. In addition, the NOAA- HYbrid Single Particle Lagrangian Integrated Trajectory (HYSPLIT) model is used to compute air parcel trajectories and model the dispersion and the route of airborne particles (Stein et al., 2015), it can be used either in a back-trajectory mode to analyze sources or in forecast mode.

2.4 Model forecast product

The National Air Quality Forecasting Capability (NAQFC) was established by NOAA in partnership with the EPA to provide operational forecasts of O_3 and $PM_{2.5}$. The NOAA-Air Resources Laboratory (ARL) and the NCEP develop upgrades for the NAQFC forecasting system, conduct and evaluate pre-implementation testing (Lee et al., 2016; Huang et al., 2017; Campbell et al., 2022). The operational

261   NAQFC consists of the NOAA-NCEP regional operational weather forecasting model, North America

262   Model (NAM) and EPA-CMAQ model before 2021 while it has been upgraded with a new dynamical core

263 known as the Finite-Volume Cubed-Sphere (FV3) in the Global Forecast System (GFS) model since
264 summer 2021 (Campbell et al., 2022). It is designed to provide 2-day model forecasts of O_3 and $PM_{2.5}$ twice
265 per day at the 06 and 12 UTC cycles. In this study, the operational NAQFC forecast products with spatial
266 resolution of 12 km at the 06 UTC cycle are used. The NAQFC performs incremental tests and evaluations
267 against the U.S. EPA AIRNow surface monitoring network. A modified version of the U. S. EPA CMAQ
268 v5.0.2 (Foley et al., 2010), is run at 12-km horizontal grid spacing with a Lambert Conformal Conic (LCC)
269 map projection for the product used in this study. The offline coupling between NWS/NCEP NAM
270 meteorological model and CMAQ is achieved by two pre-processors. In addition to the coupled
271 Nonhydrostatic Multiscale Model with Arakawa B-grid staggering (NMMB)-CMAQ system, there are
272 other components such as an emission module and chemical lateral boundary condition builder as well as
273 the products generating post-processing components. Emission inventories are processed by sectors where
274 the fire sectors include prescribed burns and wildfires in the 2017 National Emission Inventory (NEI). The
275 U.S. EPA-NEI 2014 version is processed by the interface PreMAQ for this study period. The 2006
276 Environment Canada National Inventory sources were used for the Canada-related region within the
277 NAQFC domain, and the 2012 Mexico NEI non-road sources were used for Mexico parts. The emissions
278 from wildfires, prescribed agricultural burns, and land clearing fires were computed using the dynamic fire
279 emission modeling U.S. Forest Service BlueSky smoke emission package (O'Neill et al., 2009) and the
280 NOAA-HMS for fire locations and strength. The latest version of the Biogenic Emission Inventory System
281 (BEIS) v3.6.1 is used for estimating the biogenic VOC (BVOC) emissions (Campbell et al., 2022).
282   The NAQFC CMAQv5.0.2 follows largely the U.S. EPA Aero4 module and the related emission and
283 removal processes found in the U.S. EPA-CMAQ version 5.0.2. Gas to particle conversion, heterogeneous
284 reactions, depositional growth, and coagulation are included (Kelly et al., 2009). The Aero4 module
285 simulates particle formation, condensational and coagulation growth or evaporative dissipation of existing
286 particles due to ambient chemical, temperature and humidity conditions. The Mellor Yamada Janjic (MYJ)
287 PBL scheme (Janjie et al., 2001) is used in this version of NAM. The detailed configuration for the NAQFC
288 simulations can be found in Lee et al. (2016) and Huang et al. (2017).
289   In addition, the WRF/Chem model (version 3.9.1) is used for ground O_3 and PBLH in this study (Zhao
290 et al., 2019, 2023). The grid point dimensions from the outermost to the innermost domains are 85 × 75, 76
291 × 70, and 70 × 61 with horizontal resolutions of 12 km, 4 km and 1.3 km, respectively. Outputs from the
292 Whole Atmosphere Community Climate Model (WACCM) provide initial and lateral conditions of
293 chemical species to drive the WRF/Chem simulations. This study will compare the forecast data products
294 of surface O_3 and PBLH from NOAA NAM-CMAQ (12 km resolution) and WRF-Chem (1.3 km resolution)
295 models to the observations in the NYC urban and coastal sites, and observe their performance in term of
296 their different spatial resolution. The WRF/Chem model simulations provide the hindcast data after the
297 campaign period.
298   The parameterization schemes used in the WRF/Chem simulations include microphysics scheme of Lin
299 et al. (1983), Goddard shortwave radiative transfer scheme (Chou and Suarez, 1994), Yonsei University
300 PBL scheme (Hong et al., 2006), Rapid Radiative Transfer Model longwave radiation scheme (Mlawer et
301 al., 1997). Version 2 of the Regional Acid Deposition Model (RADM2) (Stockwell et al., 1990), and Fast-
302 J photolysis scheme (Wild et al., 2000).
303   In the WRF-Chem model simulation, the Model for Ozone and Related Chemical Tracers Version 4
304 (MOZART-4/GEOS5) (Emmons et al., 2010) products are used to provide chemical initial and lateral
305 conditions to the model simulations. Anthropogenic emissions from point, on-road mobile, non-road mobile,
306 and area sources with a 4-km spatial resolution are provided by the 2014 National Emissions Inventory
307 (NEI) developed by the U.S. Environmental Protection Agency (EPA). Hourly weekday emissions for the
308 four major inventory components (point, on-road mobile, non-road mobile, and area) with a 4-km spatial

309   resolution (available at ftp://aftp.fsl.noaa.gov/divisions/taq) are used in this study. The data are currently
310   available for the contiguous 48 states of the United States, southern Canada and northern Mexico (Brioude
311   et al., 2013; Choi and Souri, 2015). Biogenic emissions are calculated using the Model of Emissions of
312   Gases and Aerosols from Nature v2.1 (MEGAN) (Guenther et al., 2012). The fire emissions inventory is
313   based on the Fire Inventory from NCAR (FINN) (Wiedinmyer et al., 2011) which provides daily average
314   of fire emissions data. More details on the model configurations and land-use categories can be found in
315   Zhao et al. (2019 and 2023); we have evaluated the WRF-Chem model predict of surface O_3 exceedance
316   for summer heat-wave event in NYC area (Zhao et al., 2019) and the O_3 profiles with ground observations
317   during LISTOS 2018 (Zhao et al., 2023).

3. Results and Discussions

3.1 O_3 episode and surface meteorology

320   **Figure 2** shows the temporal variation of ground-level O_3 and NO_2 in the NYC urban (CCNY) and coastal
321   area (Eatons Neck and Fire Island) in Long Island during July 25-31, 2019, respectively. In Fig.2 (a), the
322   O_3 concentrations show highest values at Eatons Neck in the NLI than other two sites on July 28-31, whereas
323   the O_3 concentrations are higher at Fire Island on July 25-26, 2019. In particular, the near-surface O_3 show
324   a dramatic increase from 35 ppb to 110 ppb at 8:00 am-3:00 pm (local time or EDT) and attain the maximum
325   at 100-120 ppb on July 28-30 at Eatons Neck. However, at CCNY-site the O_3 show the maximum values
326   of 60-70 ppb at 12:00-16:00 on July 28-29. In addition, in the night-time, the O_3 at Eatons Neck is generally
327   higher than at CCNY with the absolute difference of around 40 ppb on July 29-30, 2019. As one of the O_3
328   major precursors, the NO_2 at Flax Pond (Fig.2 (b)) is much lower than at CCNY and QC sites, which
329   indicates that the local photochemical production at the coastal site may not be a major source of the high
330   O_3 for this event. The maximum daily 8-hour average O_3 (MD8AO) concentrations exceed 70 ppb on July
331   28   and   29   at   Flax   Pond   in   the   North-shore   of   Long   Island
332   (https://www.dec.ny.gov/docs/air_pdf/2019o3ecx.pdf). As shown in Fig.2(c)-(d), the daily O_3 air quality
333   index (AQI) indicates the unhealthy levels in the coastal area of Long Island Sound on July 28-29, 2019.
334   **Figure 3** shows air temperature, horizontal wind speed and direction recorded at the weather station
335   of CCNY, Stony Brook (NLI) and Fire Island (SLI) on July 25-31, 2019, respectively. A heat-wave event
336   with the maximum temperature T_{max}> 32.2°C or 90°F was indicated at CCNY-site during July 28-30, 2019.
337   At Stony Brook in the NLI, air temperatures at noon and in the afternoon are clearly lower than those at
338   CCNY. As shown by the windroses maps in Fig.3(c-d) at CCNY-site, the wind directions were prevailing
339   northwest on July 25-26 but southwest in the daytime on July 28-30; this indicates that the SLI area was
340   located in the NYC downwind area on July 25-26 whereas the NLI coast and Long Island Sound were
341   located in the NYC downwind area on July 28-30. Therefore, the O_3 concentrations at the NLI and SLI area
342   are affected differently by the NYC urban emissions and pollutants transport. In addition, at Stony Brook
343   weather station in the NLI, the prevailing Northwestern and North winds were shown before 3:00 pm EDT
344   on July 28-29 (**Fig.S2 in Supporting Document**), which indicates the on-shore winds from Long Island
345   Sound or the sea-breezes to the coastal area. Thus, the high O_3 on July 28-30 at the NLI (Eatons Neck, Flax
346   Pond and Riverhead shown in Fig.S2 (e)) are associated with the combined effects from the urban pollutants
347   transport and sound-breezes that may form a convergence zone along the coast for the O_3 accumulation.
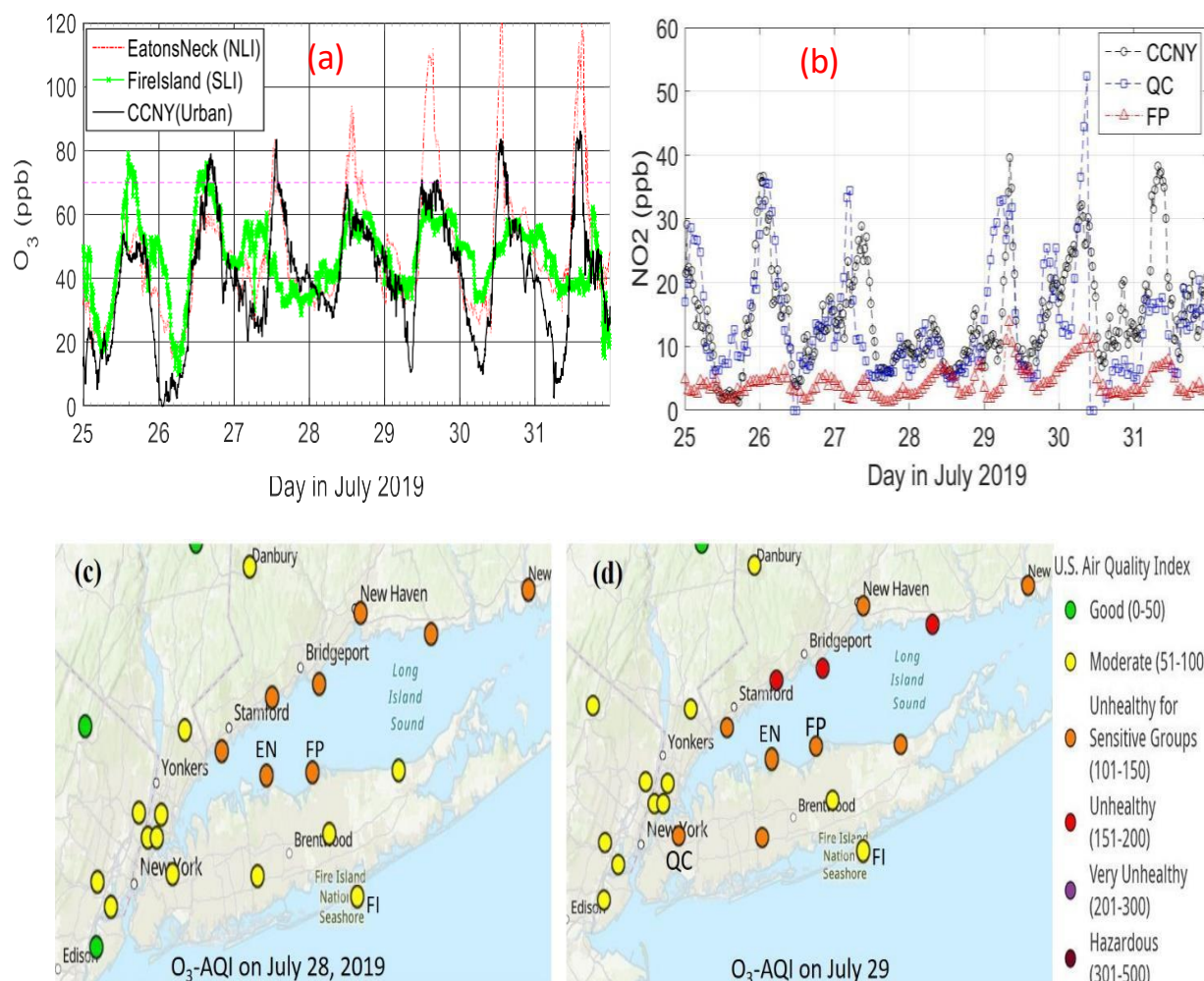
350
351

352
353
354 **Fig. 2**. Temporal variation of (a) near-surface O_3 and (b) NO_2 in the NYC urban and coastal area in Long
355 Island during July 25-31, 2019; (c)-(d) Daily O_3-AQI on July 28 and 29, 2019 from AirNow. FP-Flax
356 Pond, QC-Queens College, EN-Eatons Neck, FI: Fire Island (see Fig.1 and Table-1 for the site full names
357 and locations.)
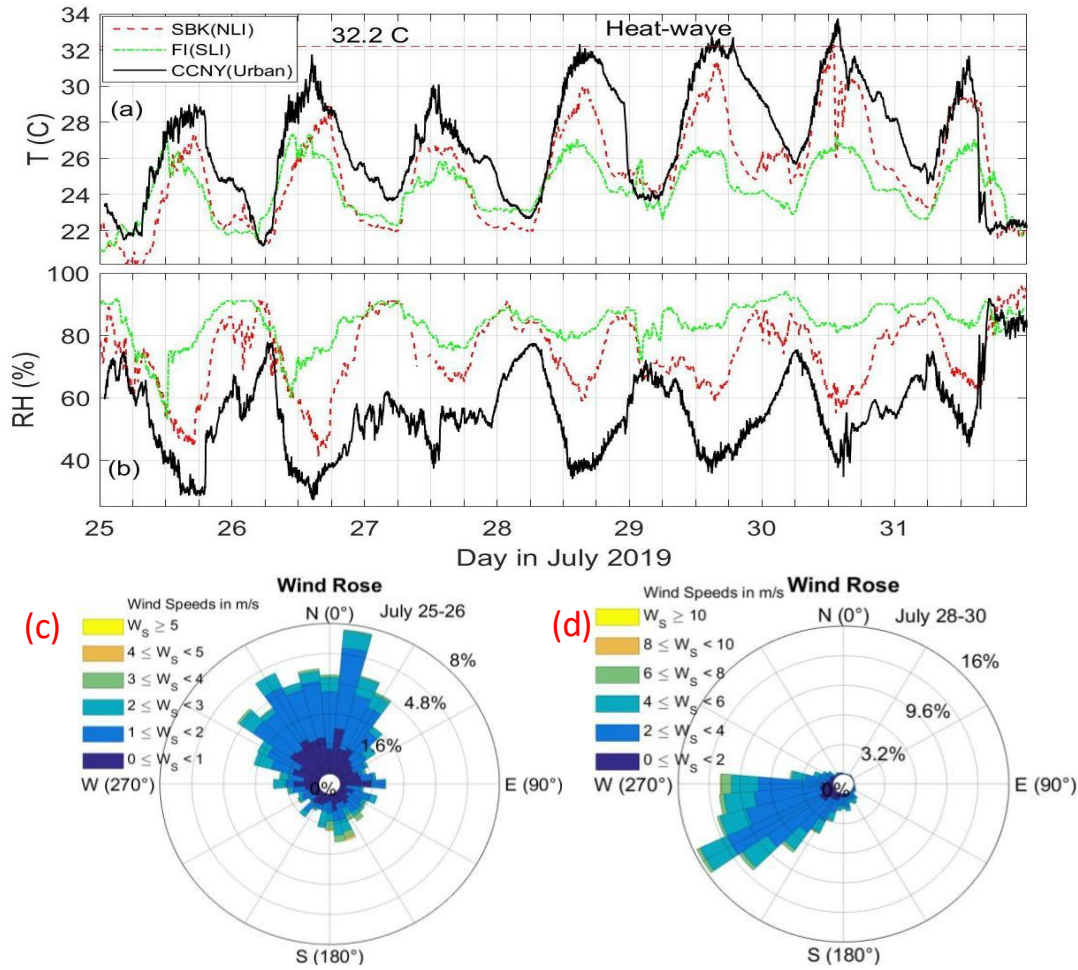
358

359

Fig. 3. (a)-(b) Air temperature and RH at CCNY (1-min ave.), Stony Brook (SBK in NLI) and Fire Island
(FI in SLI), (c) Wind rose at 6:00-18:00 EDT on July 25-26 and (d) July 28-30 at CCNY (Urban).

3.2 PBLH estimate and diurnal variation in the NYC urban and coastal area

Figure 4 shows the inter-comparison of MLH or PBLH measured from the ceilometer, wind lidar and
virtual potential temperature (VPT or θ_v) and water vapor (H_2O) profiles of the radiosonde/ozonesonde at
the NLI on July 29, 2019. The ozonesonde measured VPT and H_2O profiles at around 14:30 UTC (10:30
local time or eastern daylight time-EDT) and 19:15 UTC (15:15 local time), and the PBLH is estimated
from the sharp increase of VPT and the large decrease of H_2O mixing ratio. In the morning, the PBLH are
consistently low from these methods. For the convective boundary-layer (CBL) at 19:15-19:20 UTC, the
estimated MLH was 2.0 km from the ceilometer, 1.75 km from the wind lidar and 1.91 km from VPT profile,
respectively. Some limitations on the MLH estimate from ceilometer and wind-lidar data can be seen. For
instance, for the ceilometer data or method (Fig.4a), following the rains or shower around 4:00 UTC, some
aloft aerosol plumes at 6:00-12:00 UTC can be seen while at about 16:00 UTC there are low clouds at
around PBL-top; both aloft aerosol plumes and low-clouds induce noise on the MLH estimate. On the other
hand, the lower MLH from the wind lidar might be due to lower aerosol loading at the PBL-top (Fig.4b-
top, signal intensity or CNR). During the CBL period, the MLH estimates from the wind lidar are not
sensitive to the selected threshold values. However, for the stable boundary layer (SBL), the vertical
velocity variance method used in the wind lidar becomes incapable due to weak vertical mixing or
turbulence (Fig.4b-middle); in this case the method using the vertical gradient of horizontal wind speeds

379   can give the SBL height as shown in Fig.4b-bottom. For the CBL period on this day, the PBLHs from the
380   horizontal wind gradient method show good consistency with those from the vertical velocity variance
381   method (Correlation coefficient R=0.85). Another case study for the PBLH comparisons on July 28 is given
382   in **Fig.S3 in Supporting Document**, which shows similar comparing results in Fig.4. Table-2 lists the
383   comparisons in detail on July 28-29, 2019. Overall, the methods from the ceilometer, wind lidar and
384   potential temperature profile show good consistency of MLH for the convective PBL at noon and afternoon.
385   However, in the early morning or later afternoon, the PBLHs become lower for the stable boundary layer,
386   the different methods indicate large relative bias. On the other hand, their bias might be partially attributed
387   to different range resolutions, lowest detecting altitudes and observation locations.
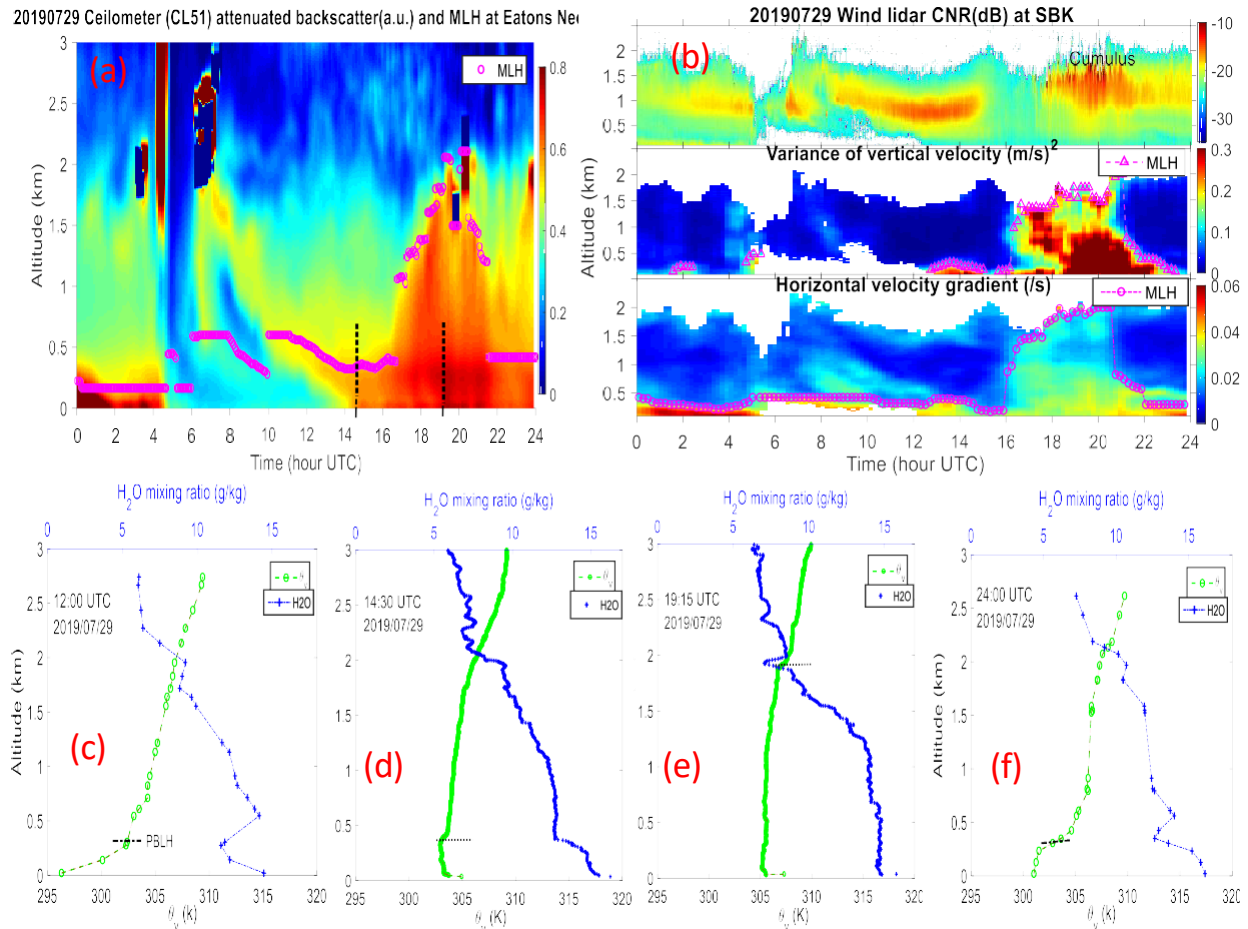
388

389

390   **Fig.4.** Comparison of MLH measured from the methods of (a) Ceilometer, (b) Wind lidar, (c–f) Virtual
391   potential temperature (θ_v) and water vapor (H_2O) profiles at the North-shore of Long Island on July 29,
392   2019. (Vertical dash lines in Fig.4 (a): ozonesonde launch time; horizontal dash lines in (c-f): PBLH)

393   **Figure 5** gives the vertical distribution profiles of aerosol total scattering coefficient at 550 nm, virtual
394   potential temperature (Θ_v), and water vapor (H_2O) measured from the UMD research aircraft near Flax
395   Pond on July 29 (time 19:32-19:52 UTC). The PBLH is calculated with the value of 1.7 km from aerosol
396   profile, 1.63 km from the Θ_v method, and 1.85 km from the vertical gradient of H_2O. They generally agree
397   well with the relative difference from the aerosol profile method less than 10%.
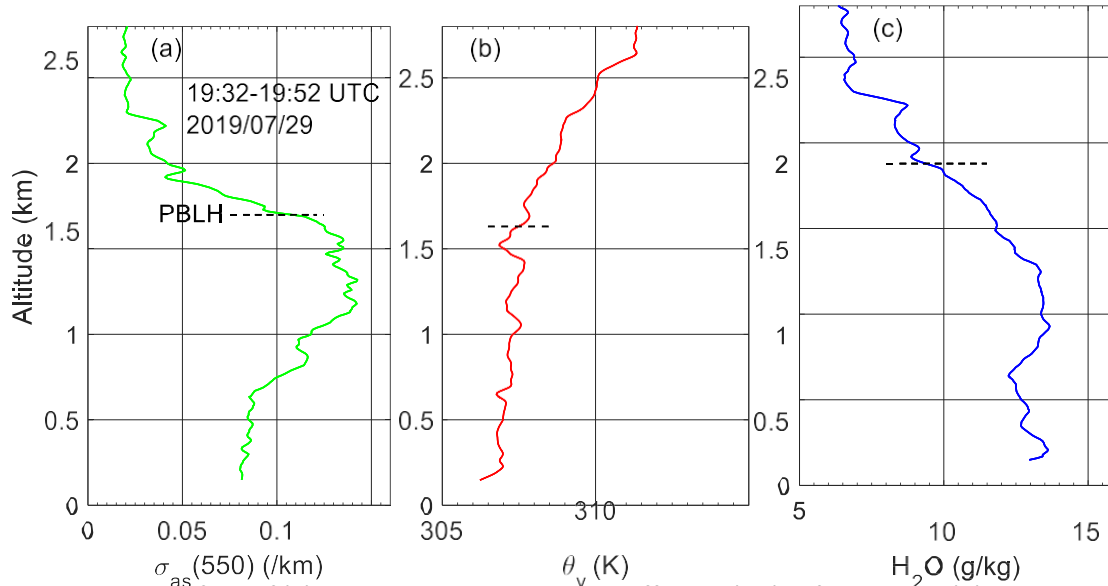
398

Fig.5. Vertical profiles of (a) aerosol total scattering coefficient (σ_{as}) at λ=550-nm, (b) virtual potential temperature (θ_v), and (c) water vapor (H_2O) measured from the UMD research aircraft near Flax Pond at 19:32-19:52 UTC on July 29, 2019. (Horizontal dash lines – PBLH estimate from each method)

Table-2. PBLH comparison among the methods from ceilometer, wind lidar and virtual potential temperature (θ_v) at the North-shore of Long Island (UTC-4=local time or EDT)

PBLH (km)	July 28 (UTC time, hour : min)			July 29 (UTC time, hour : min)			
	12:00 (SBL)	20:00 (CBL)	24:00 (SBL)	12:00 (SBL)	14:30 (CBL)	19:20 (CBL)	24:00 (SBL)
PBLHθ_v	0.38	1.94	0.37	0.30	0.38	1.91	0.33
PBLH$_{CL}$	0.36	2.01	0.35	0.52	0.335	2.05	0.41
PBLH$_{WL}$	0.30	1.80	0.40	0.20	0.30	1.75	0.20

Subscripts θ_v: Virtual potential temperature method; CL: Ceilometer method; WL: Wind lidar method. The PBLH is equivalent to MLH for the Convective Boundary Layer (CBLH) (Stull, 1988).

Figure 6 gives the ceilometer-measured attenuated backscatter intensity and MLH and at CCNY, Eatons Neck and Fire Island during July 26-31, 2019, respectively. These backscatter intensities are relative values since they are not yet calibrated with the instrument constant. It can be seen that the MLHs increase from 0.3 to 2.0 km at 10:00 am to 2:00 pm EDT on July 28 and 29 at CCNY; and the maximum MLH is much higher at CCNY (~2.0 km) than at Eatons Neck (~1.65 km) on NLI and Fire Island on SLI. The MLH is at the lowest level at Fire Island along with residual aerosol layers (aerosol layer height - ALH in Fig.6c), which corresponds to much lower air temperature (Fig.3a). In addition, at these three-site, the aloft aerosols plumes and low-clouds can be seen on July 27-31, and some rain or showers occurred in the early morning of July 29, noon on July 30 and 31. Unfortunately, there are no data records at Eatons Neck from the night of July 29 to noon of July 30 due to the data transfer issue from the instrument to computer. Below we focus on the comparison analysis of MLH and O_3 in the NYC urban and North-shore of Long Island (NLI) on July 28-30, 2019 since the ground O_3 are at the highest levels in the NLI and there are the O_3 and meteorological profile data available from the ozonesonde and UMD research aircraft in the NLI.

14
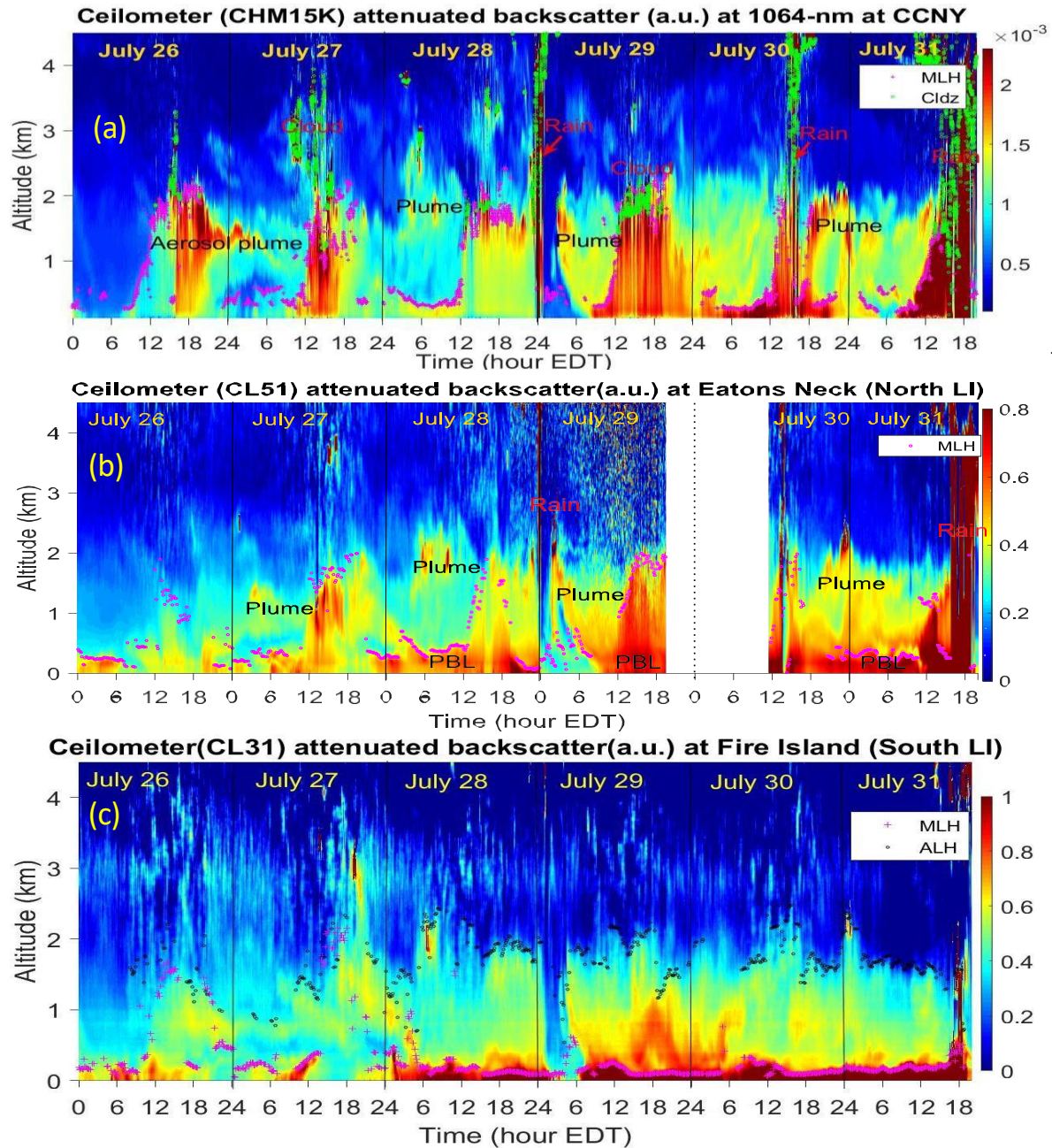
Fig. 6. Ceilometer-measured backscatter intensity (relative values) and MLH at (a) CCNY, (b) Eatons Neck, and (c) Fire Island during July 26-31, 2019. (MLH: mixing-layer-height; Cldz: cloud base; ALH: aerosol-layer-height)

We made the comparison and correlation analysis of the MLH between the ceilometer and wind lidar methods at the NYC urban and NLI coastal area on July 28-30, 2019, respectively. **Figure 7** shows their temporal variations and the linear regression. At both two areas, the MLHs from the ceilometer and wind lidar show consistent diurnal variation. In the NYC urban area as shown in Fig.7b, the MLHs from the ceilometer and wind lidar show strong linear correlation with the regression slope of 0.99 and correlation coefficient of R=0.9. In the coastal area in NLI as shown in Fig.7d, the MLHs in the convective PBL period are slightly underestimated from the wind lidar in comparison to the ceilometer, their linear correlation coefficient is 0.81 and the linear regression slope is 0.67. In the coastal area, the vertical convection intensity

15

434 is relatively weak and the aerosol loadings are less than those in the urban area, thus the estimated MLHs
435 from the wind lidar and ceilometer show a moderate correlation and reasonable consistency.
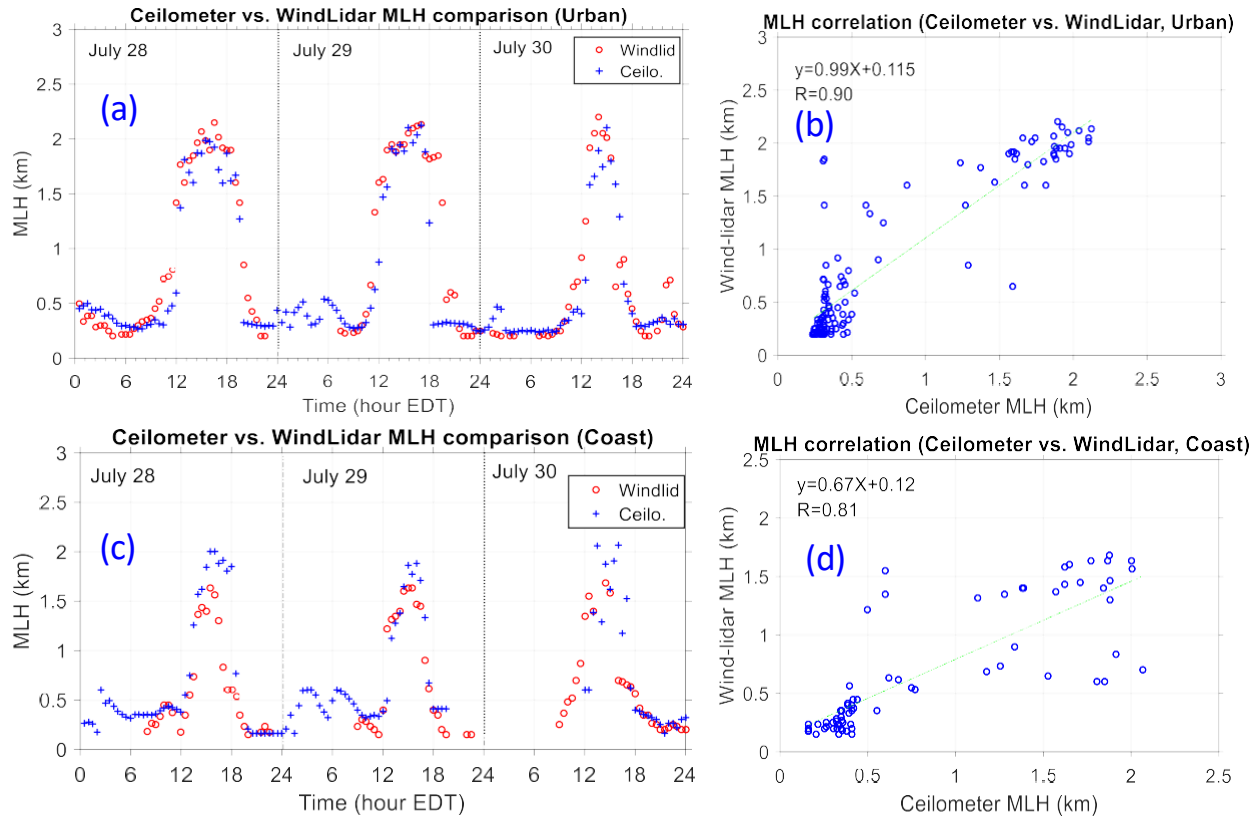

436

437

438 **Fig. 7.** Comparison and correlation of MLH (30-min ave.) between the ceilometer and wind-lidar
439 methods in the NYC urban (a-b), and the NLI coastal area (c-d), respectively.

440   **Figure 8** shows the diurnal variation and comparison of ground-level O_3 and MLH in the NYC urban
441 and coastal area in NLI on July 28-30, 2019. In comparison to the NYC urban area, the maximum O_3
442 concentrations are much higher in the coastal area (Fig.8a) whereas the MLHs are much lower at noon and
443 in the afternoon (Fig.8b). Meanwhile, the MLHs start to grow earlier from the mid-morning to noon in the
444 urban area than the coastal area (Fig.8b). High MLH in the urban area is generally due to hot surface and
445 strong vertical mixing. As shown in Fig.8c, the ratios of vertical velocity variances at the urban to those in
446 the coastal area indicate much stronger vertical convection during the PBL transition periods (10:00-13:00
447 and 17:00-19:00 EDT) in the urban area. As for July 29, the MLH grows from 0.25 to 2.0 km altitude at
448 10:00-11:30 EDT in the urban area, but rises from 0.2 to 1.7 km from 12:00 to 15:00 EDT in the coastal
449 area. At noon and early afternoon (convective PBL), the average MLH is at 2.0±0.1 km at 13:00-17:00
450 EDT in the urban area, but becomes lower with the average of 1.5 ± 0.14 km at 13:00-16:00 EDT in the
451 coastal area. During the time period above, the ground O_3 concentrations keep increasing in the coastal area
452 but become stable in the urban area (Fig.8a). Lower MLHs in the coastal area indicate smaller air volumes
453 for the O_3 dilution or dispersion thereby partially resulting in higher O_3 at near-surface.
454   We calculated the integrated O_3 content (IOC) in the PBL at noon time when both PBL height (PBLH)
455 and surface O_3 attain the maximum values. The O_3 might be assumed to be well mixed due to strong
456 turbulence mixing in the PBL. Subsequently, the integrated O_3 content (IOC) in the PBL at noon can be
457 calculated with the PBLH or MLH multiplying surface O_3 concentration. The comparison of IOC may
458 indicate the PBL-height impact on the surface O_3 at noon since the PBLH generally defines the air volume

459   for surface O_3 dilution. However, the uncertainty of such comparison depends on the O_3 vertical distribution
460   and local chemical process for O_3 production. On July 28 (14:00-16:00 EDT), the average IOC is 114.8 ±
461   6.3 ppb×km at CCNY-site (urban) and 112.4 ± 11.2 ppb×km at Eatons Neck (coast), respectively. On July
462   29 (13:00-16:00 EDT), the average IOC is 127 ± 9.9 ppb×km at CCNY and 159 ± 20 ppb×km at Eatons
463   Neck. Therefore, they generally show good consistency at noon time in the urban and coastal area.
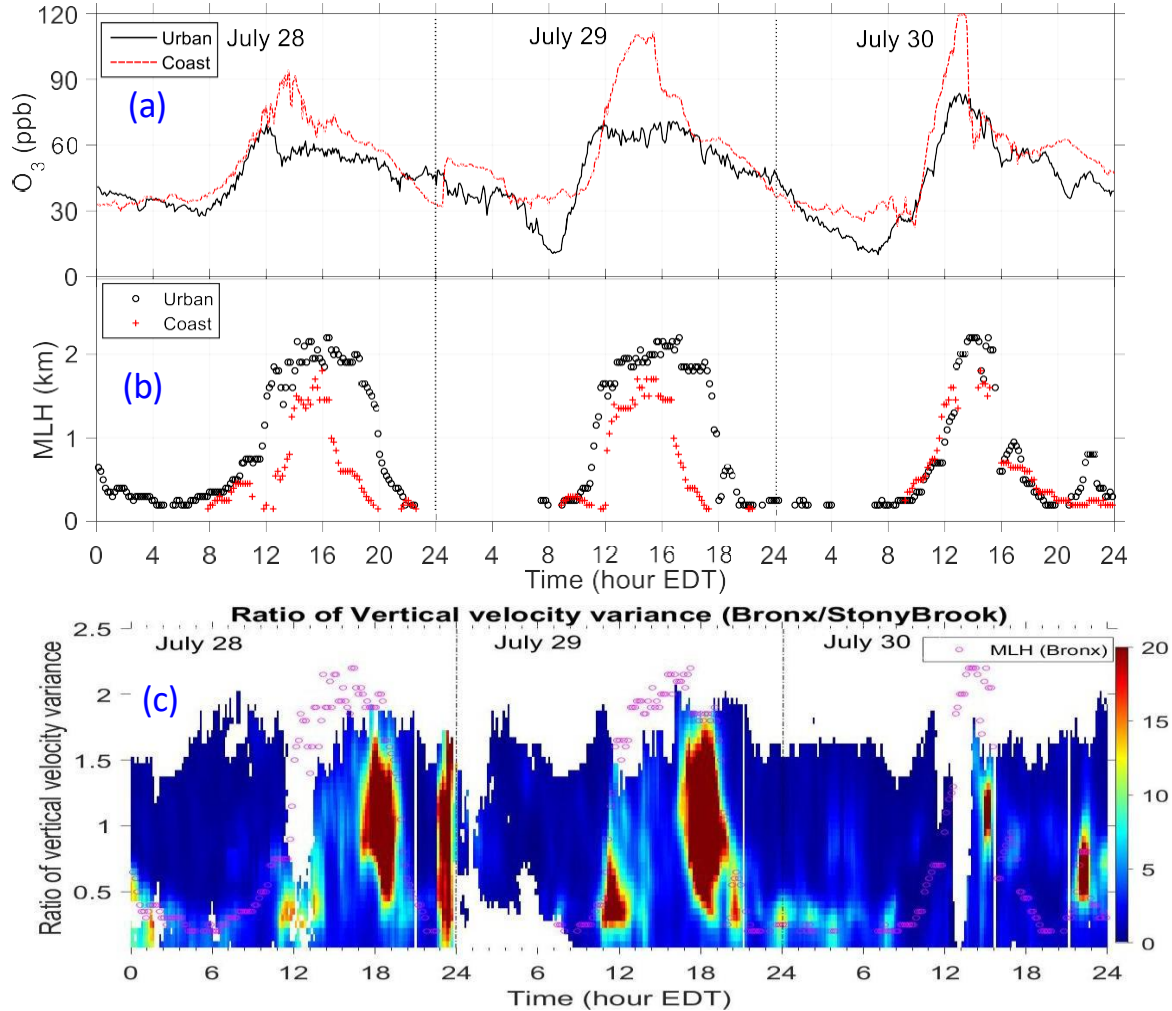
464

465
Fig. 8. Diurnal variation of ground O_3 (a), MLH (b), and (c) Ratio of vertical velocity variance from the
wind lidar measurements in the NYC urban and the coastal area in North-shore of Long Island (NLH) on
July 28-30, 2019 (red circles: MLH in the urban area).

469

470   ## 3.3 Horizontal winds and vertical mixing in the PBL

471   **Figure 9 and 10** show the wind-lidar measured backscattering intensity or carrier-noise-ratio (CNR),
472   horizontal wind speed, direction, and vertical velocity in the NYC urban and the coastal area in NLI during
473   July 28-31, 2019, respectively. Fig.9 (a) indicates the lidar detection altitude, cloud and rain information
474   (stronger backscatter). First, the horizontal wind directions indicate the prevailing southwest (SW) in the
475   NYC urban area (Fig.9c) but the northwest (NW) before 15:00 EDT in the lower PBL at Stony Brook
476   (Fig.10c) on July 28 and 29. This means that the NLI area suffers from the downwind transport of NYC
477   urban plumes; meanwhile, the prevailing Northwest winds below 0.4 km altitude at 10:30-15:00 EDT on
478   July 28-29 in Fig.10(c) indicate the sea breezes from Long Island Sound that prevent the off-shore

17

479   dispersion of the pollutants. In addition, the surface weather observations at the Stony Brook campus also
480   indicate that the prevailing NW winds occur before 15:00 EDT on July 28 and 29, 2019 (**Fig.S2 in**
481   **Supporting Document**). Furthermore, the vertical velocity variances indicate much weaker vertical mixing
482   in the NLI than those in the NYC urban area (not shown here), particularly in the time period of MLH
483   morning transition. Therefore, the urban pollutants transport, low MLH, weak vertical mixing and sea-
484   breezes provide the beneficial meteorological conditions for the O_3 accumulation in the North-shore of
485   Long Island. The chemical production and deposition process of O_3 may also affect spatial patterns of O_3
486   in the coastal area, which is out of the scope of this paper.
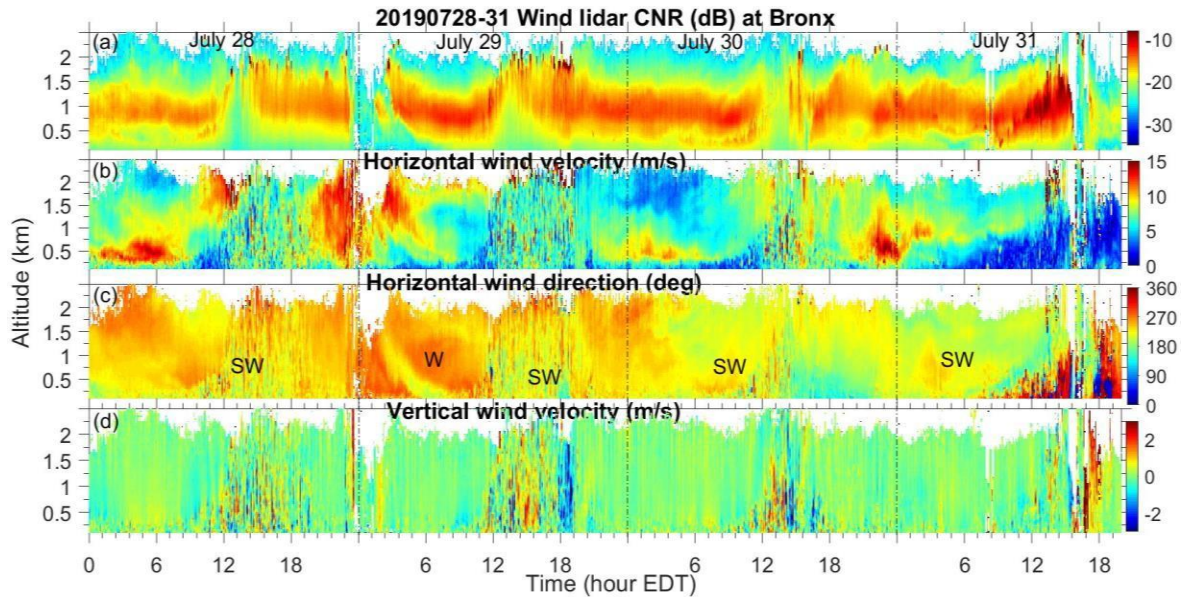

487
488   **Fig.9**. (a) Wind lidar measured carrier-noise-ratio (CNR), (b) horizontal wind speed, (c) wind direction,
489   (d) vertical wind velocity (+up, –down) at Bronx (NYC urban site) during July 28-31, 2019.
490
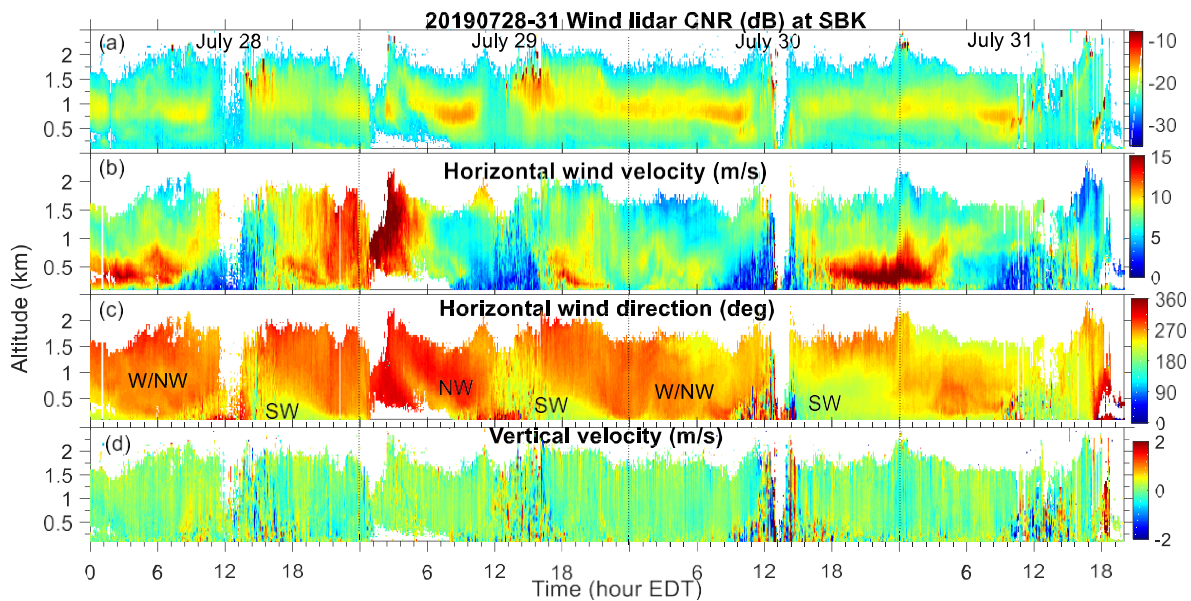
491
492   **Fig.10**. Same as Fig.9 except at Stony Brook (SBK) in the Northern Long Island (NLI). (The prevailing
493   Northwest winds below 0.4 km altitude at 10:30-15:00 EDT on July 28-29 in Fig.10(c) indicate the sea
494   breezes from Long Island Sound, please refer to the site location in Fig.1.)

18

3.4 Vertical profiles of O_3 and other gaseous compounds

Figures 11 and 12 show the vertical distribution of O_3 and winds measured from the ozonesondes at Flax Pond on July 29, 2019 (14:29-14:40 UTC in the morning and 19:14-19:22 UTC in the afternoon), respectively. The corresponding virtual potential temperature and H_2O profiles are referred in Fig.4 (d)-(e). The O_3 mixing ratio profile shows slight variation below 3-km altitude in the mid-morning with the concentration of 60-62 ppb (Fig.11a); prevailing winds are out of the NW near the surface (Fig. 11b). However, a significant increase of the O_3 can be seen with the mixing ratios of 83-102 ppb in the afternoon (Fig.12a). Moreover, Fig.12a indicates higher O_3 in the upper PBL than at near-surface (<0.5 km), which might be associated with the dramatic variation of horizontal wind direction and speed (prevailing SSW and weak winds below 0.5 km but WSW stronger speed above 0.5 km).
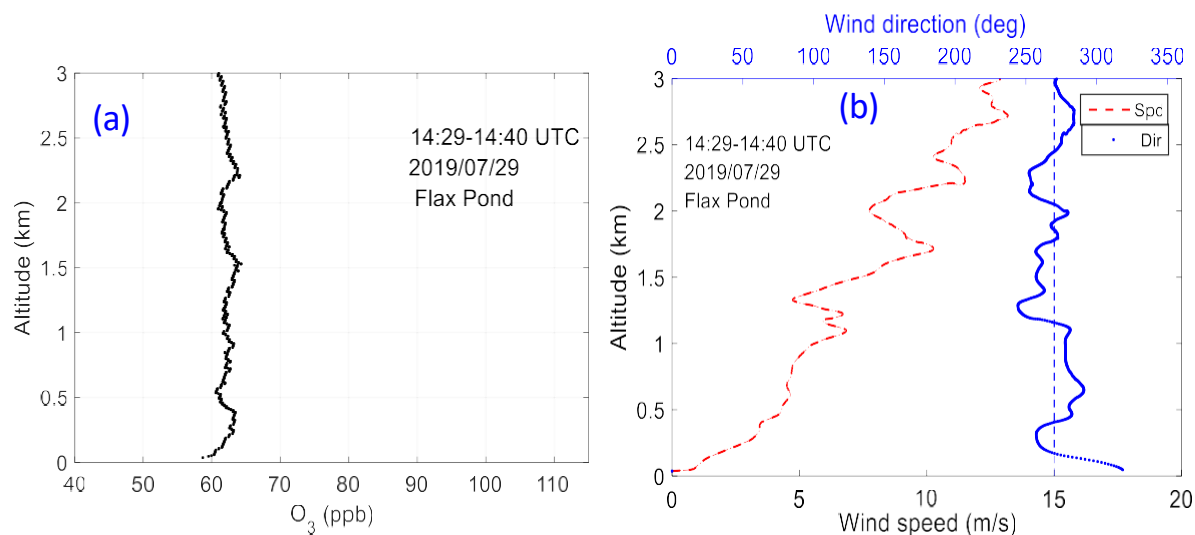
Fig.11. (a) Vertical distribution of O_3, (b) wind speed (Spd) and direction (Dir.) measured from the ozonesonde at 14:29-14:40 UTC on July 29, 2019 (vertical dash: wind direction at 270°).


Fig. 12. (a)-(b) Same as Fig.11 except at 19:14-19:22 UTC on July 29, 2019 (afternoon).

19
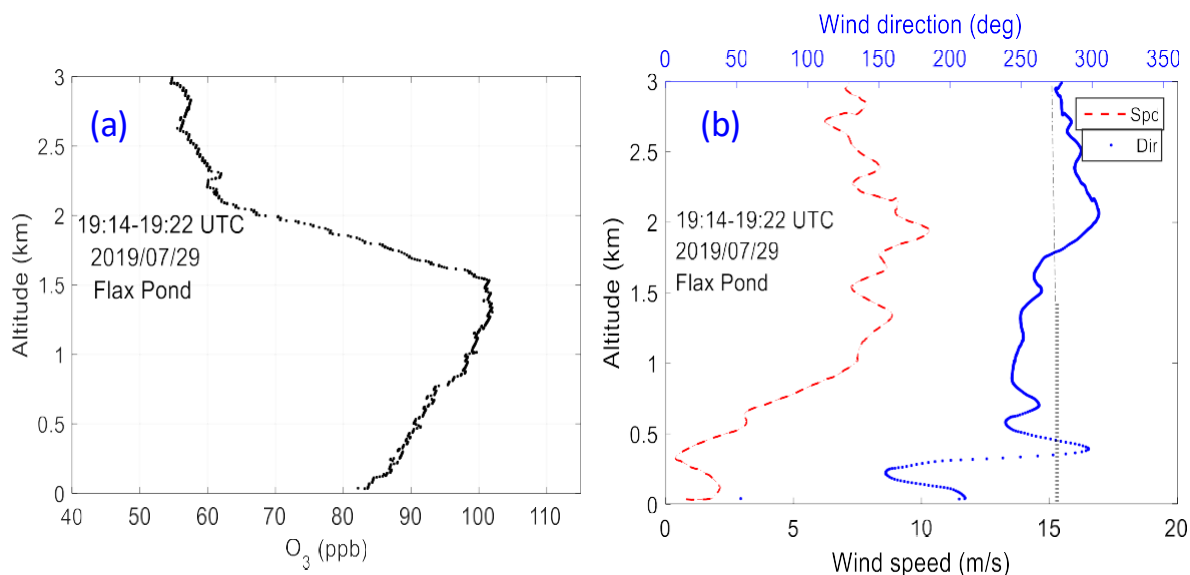
510   **Figure 13** shows the vertical distribution of O_3, CO, NOx, HCHO, and aerosol scattering coefficient
511   measured by the UMD research aircraft in the afternoon of July 29, 2019; and the corresponding flight track
512   and time-height are given in Fig. 13(a). The flight time for the two vertical profiles (aircraft spiral up and
513   down) is at 19:32-20:15 UTC; the ascent (green track in Fig. 13a and P1 in Fig. 13 (b-g)) is located nearby
514   Flax Pond on the North-shore of Long Island while the descent (red track in Fig. 13a and P2 in Fig. 13 (b-
515   g)) starts from the North-shore of Long Island, then crosses Long Island Sound and finally lands inland on
516   Long Island. As shown in Fig. 13 (b), the O_3 mixing ratios are much higher with the value of 110-120 ppb
517   in the PBL in the North-shore of Long Island (P1-green) than other area (P2-red). Concentrations of CO,
518   NOx, HCHO, CH_4, and aerosols are also higher over the North-shore of Long Island (Fig.13(c-g)). Ozone
519   shows slight variability in the PBL whereas the aerosols and other gaseous compounds show a little larger
520   values at 0.6 km-1.5 km altitude than those below 0.5 km altitude. The larger aerosol backscatters could be
521   related to the local RH maximum. Profiles of black carbon (BC), virtual potential temperature, and water
522   vapor are given in **Fig. S4 in the Supporting Document**, these indicate more BC over NLI. These
523   coincident high-levels of O_3, CO, NO_x and HCHO in the PBL indicate the transported urban plumes; and
524   the high-level O_3 agrees well with the ground measurements at Eatons Neck and Flax Pond in NLI area but
525   differ from the ozonesonde measured O_3 profile near the surface (inland of LI) (**Fig.12**). The spatial
526   homogeneity of O_3, CO, NO_2 and BC is illustrated from the low-level flight measurements (e.g., flight
527   altitude **at 0.15-0.36 km at 18:32-20:22 UTC** in the afternoon on July 29), and the results indicate higher
528   concentrations of O_3, CO and BC near the Shoreline along Eatons Neck and Flax Pond (**See Fig.S5 in**
529   **Supporting Document**); the CO and BC concentrations are even higher in the North-shoreline of LI than
530   those near NYC urban area. In addition, the transported wildfire smoke plumes are indicated from the lidar-
531   ceilometer and NOAA fire and smoke product (**See Fig.15 below and Fig.S6 in Supporting Document**)
532   in NYC urban and Long Island Sound area, which may indicate the urban plumes mixing with the
533   transported smoke in the NYC and Long Island Sound area.
534

3.5 Spatial distribution of NO_2, HCHO and aerosols from satellite sensors

536   **Figure 14** gives the spatial distribution of tropospheric column contents of NO_2 and HCHO measured from
537   satellite S5P/TROPOMI on July 28 and 30, 2019 (no retrievals available on July 29). The results indicate
538   higher NO_2 and HCHO in the NYC urban area and North-shore of Long Island on both days, which is
539   qualitatively consistent with higher NOx and HCHO concentrations in the PBL observed by the UMD
540   aircraft around Flax Pond. In addition, the satellite MODIS/Aqua RGB images show clear sky over Long
541   Island Sound but a line of clouds in Long Island (**Fig.S7 in Supporting Document**), which generally
542   indicates the sea-breeze front (Bao et al., 2023). Therefore, higher NO_2, HCHO, CO and aerosols from the
543   aircraft and satellite data likely indicate a convergence zone in the North-shore of Long Island where the
544   transported O_3 and other urban pollutants could be accumulated.
545
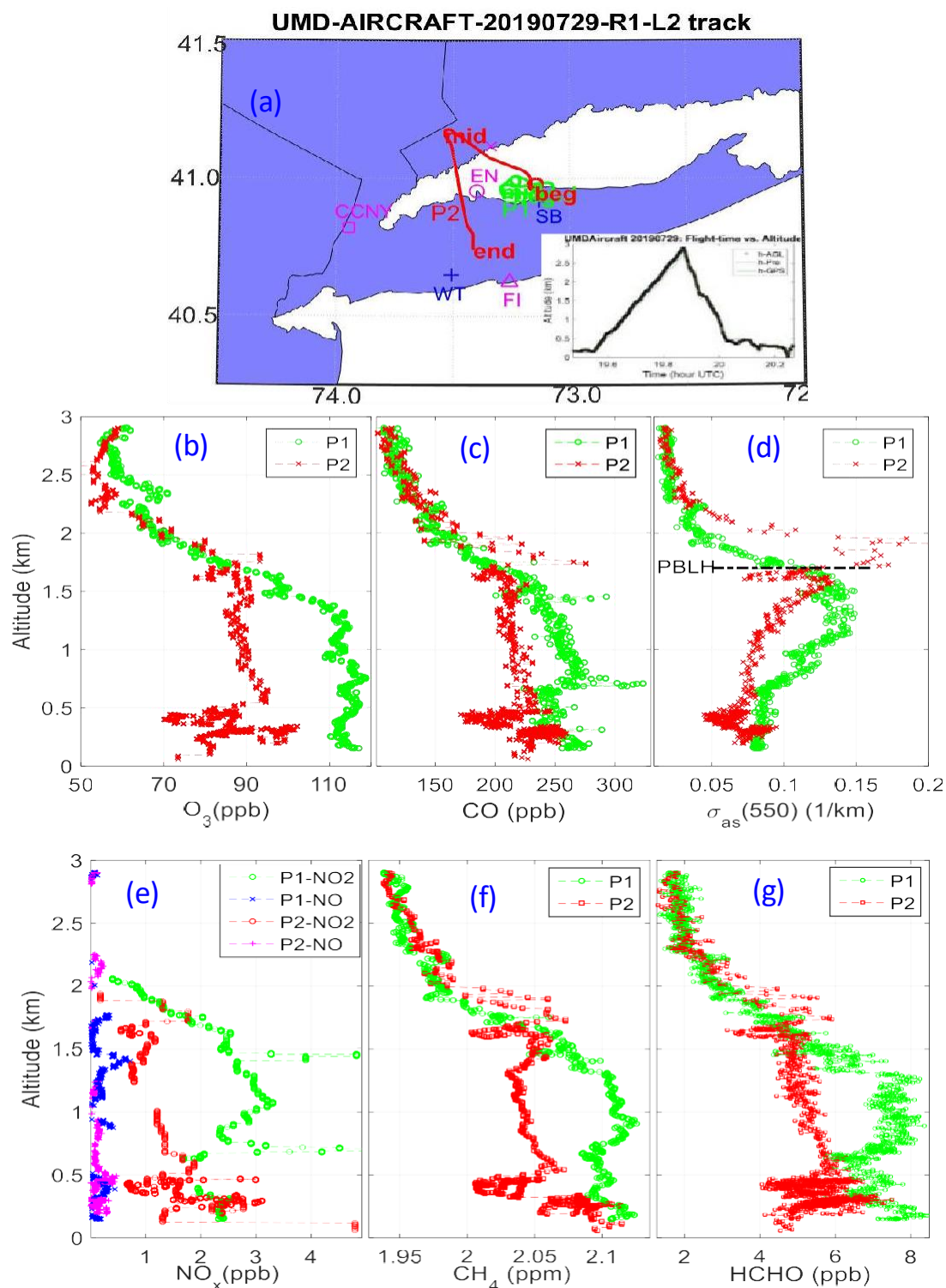
Fig.13. (a) Aircraft flight track and time-height for the two vertical profile measurements (P1- ascent in green; P2- descent in red), (b)-(g) Profiles of O_3, CO, aerosol scattering coefficient (σ_{as}, horizontal dash-PBLH), NO_x, CH_4, HCHO on July 29, 2019. P1: ascent at 19:32-19:52UTC near Flax Pond; P2: descent at 19:52-20:15UTC cross LIS.
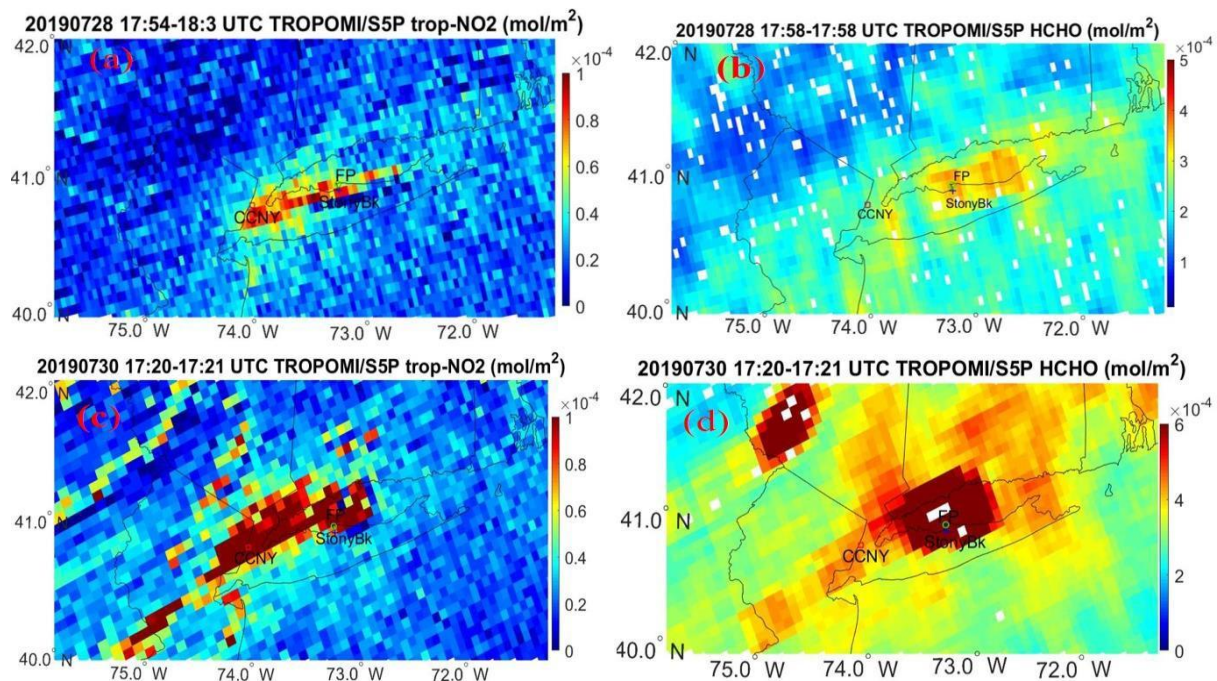
Fig.14. (a)-(d). Tropospheric column content of NO_2 and HCHO measured from S5P/TROPOMI/ on July 28 (a, b) and 30, 2019 (c, d).

In addition, the transported wildfire smoke plumes were indicated by CALIPSO and NOAA-HMS Fire and Smoke product as shown in Fig.S8 in the Supporting Document. **Fig.S8** (a)-(b) shows the range-resolved total attenuated backscatter and aerosol types measured from the satellite CALIPSO in the east coastal area around NYC in the early morning of July 30 (2:00 am local time) or in the late night of July 29, 2019. The results indicate some aloft smoke plumes in the PBL that are classified by aerosol optical properties around the NYC and LIS area. Furthermore, the NOAA Hazard Mapping System (HMS) fire and smoke product indicates the smoke intrusion (light-moderately dense) to the NYC area (Fig.S8c), the lighter density (usually far downwind) HMS smoke polygons are decoupled from the surface (Liu et al, 2023). In addition, the NOAA-HYSPLIT ensemble backward trajectories show that the air at 2-km altitude at CCNY mostly originated from the Northwest US and Canada and traveled for 7-days. On the other hand, the NOAA HRRR-smoke model forecast shows light-moderate levels of smoke intrusion to the NYC/LIS region during July 26-29, 2019 (the images available at https://rapidrefresh.noaa.gov/hrrr/HRRRsmoke/). In addition, the wildfires and smoke plume were observed on July 22-25, 2019 in the Northwest US during the FIREX-AQ campaign (Crawford, et al., 2021; June et al., 2022). Overall, these satellite observations and the model predicted results demonstrate high levels of NO_2, HCHO and aerosols in the North-shore of Long Island, and indicate the transport of the NYC urban plumes and the aged wildfire smoke plumes.

3.6 Evaluation of WRF-Chem and NOAA NAM-CMAQ modeling O_3 and PBLH

At last, we made the comparisons of ground O_3 and PBLH between the WRF-Chem model (1.3 km grid), NOAA NAM-CMAQ (12 km grid) model forecast and the observations at the coastal area in Long Island (Riverhead and Babylon sites) and NYC urban area (CCNY-site) during July 28-30, 2019. **Fig.15** shows the comparisons of O_3 at Riverhead and Babylon sites. It can be seen that there is a time-lag of 2-3 hours for the maximum O_3 timing from the NAM-CMAQ model, but the WRF-Chem products show good consistency with the observations. In addition, at the coastal site as shown in Fig.15c, the PBLH from the NAM-CMAQ model are generally lower than the observation data at noon and in the afternoon. During the morning transition period or PBLH growing period, the PBLHs from the NAM-CMAQ model product start

22

581 to grow earlier than the observation data, which might partially affect the predicted O_3 concentrations near
582 the surface. On the other hand, in the urban area (CCNY-site), the NAM-CMAQ modeled O_3 values show
583 consistent timing for the maximum O_3 with the observation (See **Fig.S9 in the Supporting Document**).
584 However, the night-time O_3 from the WRF-Chem predictions are over-estimated. In addition, the
585 comparisons of the air temperature and wind between the models and observations at CCNY are shown in
586 **Fig. S10 in the Supporting Document;** and the results indicate that the modeling temperature and
587 horizontal wind direction agree well with the observation whereas the horizontal wind speeds are over-
588 predicted by the model. Torres-Vazquez (2022) evaluated the WRF-CMAQ simulation performance of the
589 meteorology and O_3 for LISTOS 2018, and the two cases studies suggest that higher spatial resolution (1.3
590 km grid) improved surface meteorology simulation throughout the whole summer. Further sensitivity and
591 comparison analysis of the model simulations are highly recommended with different spatial resolutions,
592 emissions and meteorological initiation at the coastal area, this is out of this study and will be explored in
593 a separate research.
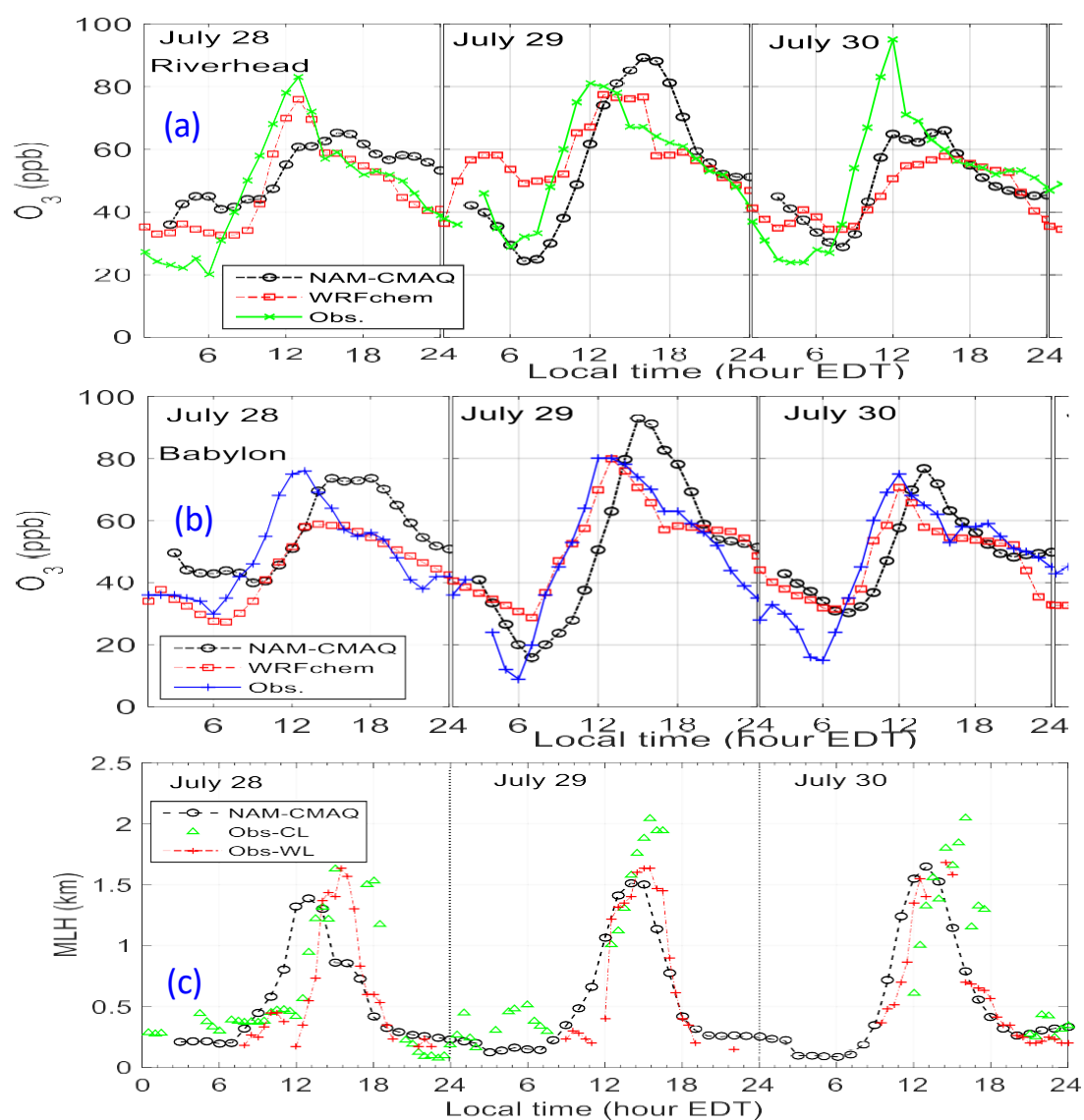
594

595

596

597 **Fig.15** (a)-(b) Comparisons of ground-level hourly O_3 between the WRF-Chem, NAM-CMAQ model and
598 the observations, (c) MLH comparison in the coastal area of Long Island during July 28-30, 2019.

4. Conclusions

This study presents the integrated observations and comparisons of O_3 and PBLH diurnal variation in New York City and its downwind coastal area in Long Island Sound. The multi-platform measurements are used to investigate the PBL dynamics for a persistent O_3 episode during July 28-31, 2019, which includes the research aircraft, wind lidar, ceilometer, aerosol lidar, ozonesonde and in-situ samplers. The results indicate that higher O_3 in the North-shore of Long Island (NLI) is associated with lower PBLH, urban pollutant transport and land-sea breezes.

For the convective boundary layer, the methods from the ceilometer, wind lidar and potential temperature profile obtain consistent PBLH or MLH by showing their absolute differences at around 100-200 m and strong correlation (R>0.8). However, for the stable boundary layer in the morning and night in the NLI, it becomes a challenge to estimate the low PBLH using the variance of vertical velocity whereas the method with the vertical gradient of horizontal wind speed can obtain a reasonable result. The ceilometer can report a reasonable PBLH except for some contamination or noises from aloft aerosols and low clouds. In addition, the PBLHs are generally lower in the mid-morning and noon in the NLI than the NYC urban area whereas the ground-level O_3 are much higher in the NLI area than the urban area. However, the total O_3 in the PBL defined as the O_3 concentration multiplied PBLH indicate similar values at noon in the NYC urban and NLI coastal site on July 28-29, 2019.

Coincident high-levels of O_3, CO, NO_x, HCHO, CH_4, aerosols and BC were observed in the PBL in the NLI area; they show horizontal in-homogeneity at lower altitude (150-360 m AGL) in LIS area, this is further indicated from the satellite TROPOMI-measured tropospheric column NO_2 and HCHO. In addition, light-moderate levels of the transported wildfire smoke were indicated in the PBL from the lidar/ceilometer observations, satellite CALIPSO, NOAA-HMS fire and smoke product, and HRRR-smoke model prediction in NYC and LIS area. Overall, high O_3 levels in the NLI may be attributed to the complex impacts of the urban plumes transport, lower PBLH and land-sea breezes. This study does not discuss the chemical production and deposition process of O_3 that may also affect spatial patterns of O_3 in the coastal area, which is out of the scope of this paper.

In comparison to the observations, both the NOAA NAM-CMAQ and WRF-Chem models show good consistency of ground O_3 and PBLH at the NYC urban site. But in the North-shore of Long Island (NLI), the NOAA NAM-CMAQ model forecast (12-km grid) illustrates a timing delay of 2-3-hr for the maximum O_3 while the WRF-Chem predictions (1.3-km grid) show good consistency for the maximum O_3 timing. The NAM-CMAQ model indicates that the PBLH grows later in the morning and is lower at noon than the observations. Further sensitivity analysis of the model simulations are highly needed with different spatial resolutions, emissions and meteorological initiation at the coastal area in the future.

References

647   Abdi-Oskouei, M., Carmichael, G., Christiansen, M., Ferrada, G., Roozitalab, B., Sobhani, N., Wade, K.,
648   Czarnetzki, A., Pierce, R. B., Wagner, T., Stanier, C, 2020. Sensitivity of meteorological skill to
649   selection of WRF-Chem physical parameterizations and impact on ozone prediction during the Lake
650   Michigan Ozone Study (LMOS). J Geophy. Res. (Atmos.), 125 (5), e2019JD031971,
651   https://doi.org/10.1029/2019JD031971.

652   Angevine, W., White, A. B., Senff, C.J., Trainer, M., Banta, R.M., Ayoub, M.A. 2003. Urban-rural
653   contrasts in mixing height and cloudiness over Nashville in 1999. J. Geophys. Res., 108 (D3) 4092,
654   doi: 10.1029/2001/JD001061.

655   Angevine, M. W., Zagar, M., Tucker, S. C., Fairall, C. W., Bariteau, L., Wolfe, D. E., Brewer, W. A.
656   2008. Modeling the boundary layer over Galveston Bay and the Gulf of Mexico for air pollution
657   studies, 18th Symposium on Boundary Layers and Turbulence, 16A.1.

658   Bao, S., Pietrafesa, L., Gayes, P., Noble, S., Viner, B., Qian, J.-H., et al. (2023). Mapping the spatial
659   footprint of sea breeze winds in the southeastern United States. J. Geophy. Res.: Atmos., 128,
660   e2022JD037524. https://doi.org/10.1029/2022JD037524

661   Brotzge, J. A., Wang, J., Thorncroft, C. D., Joseph, E., Bain, N., Bassill, N., Farruggio, N., Freedman, J.
662   M., Hemker, K., Jr., Johnston, D., Kane, E., McKim, S., Miller, S. D., Minder, J. R., Naple, P.,
663   Perez, S., Schwab, J. J., Schwab, M. J., Sicker, J. 2020. A Technical Overview of the New York
664   State Mesonet Standard Network, Journal of Atmospheric and Oceanic Technology, 37(10), 1827-
665   1845, https://doi.org/10.1175/JTECH-D-19-0220.

666   Caicedo, V., Rappenglueck, B., Cuchiara, G., Flynn, J., Ferrare, R., Scarino, A.J., Berkoff, T., Senff, C.,
667   Langford, A., Lefer, B., 2019. Bay-breeze and sea breeze circulation impacts on the planetary
668   boundary layer and air quality from an observed and modeled DISCOVER-AQ Texas case study. J.
669   Geophys. Res.: Atmosphere 124, 7359–7378. https://doi.org/10.1029/2019JD030523.

670   Caicedo, V., Delgado, R., Sakai, R., Knepp, T., Williams, D., Cavender, K., Lefer, B., Szykman, J., 2020.
671   An Automated Common Algorithm for Planetary Boundary Layer Retrievals Using Aerosol Lidars
672   in Support of the U.S. EPA Photochemical Assessment Monitoring Stations Program, J. Atmos.
673   Oceanic Technol., 37(10), 1847-1864.

674   Caicedo, V, Delgado, R., Luke, W., Ren, X., Kelley, P., Stratton, P., Dickerson, R., Berkoff, T., Gronoff,
675   G., 2021. Observations of bay-breeze and ozone events over a marine site during the OWLETS-2
676   campaign, Atmos. Environ. 263, 118669, https://doi.org/10.1016/j.atmosenv.2021.118669

677   Campbell, P. C., Tang, Y., Lee, P., Baker, B., Tong, D., Saylor, R., Stein, A., Huang, J., Huang, H.-C.,
678   Strobach, E., McQueen, J., Pan, L., Stajner, I., Sims, J., Tirado-Delgado, J., Jung, Y., Yang, F.,
679   Spero, T. L., Gilliam, R. C., 2022. Development and evaluation of an advanced National Air Quality
680   Forecasting Capability using the NOAA Global Forecast System version 16, Geosci. Model Dev.,
681   15, 3281–3313, https://doi.org/10.5194/gmd-15-3281-2022.

682   Castellanos, P., Marufu, L. T., Doddridge, B. G., Taubman, B. F., Ehrman, S. H., Dickerson, R. R., 2011,
683   Ozone, nitrogen oxides, and carbon monoxide during pollution events over the eastern US: An
684   evaluation of emissions and vertical mixing, J. Geophys. Res., 116, D16307,
685   doi:10.1029/2010JD014540.

686   Coggon, M. M., Gkatzelis, G. I., McDonald, B. C., Gilman, J. B., et al., 2021. Volatile Chemical Product
687   Emissions Enhance Ozone and Modulate Urban Chemistry. Proc. Natl. Acad. Sci., 118,
688   e2026653118.

689   Couillard, M. H., Schwab, M. J., Schwab, J. J., Lu, C.-H., Joseph, E., Stutsrim, B., 2021. Vertical profiles
690   of ozone concentrations in the lower troposphere downwind of New York City during LISTOS
691   2018–2019. J. Geophy. Res. (Atmos.), 126, e2021JD035108. https://doi.org/10.1029/2021JD035108.

692   Crawford, J. H., C. Warneke, J.P. Schwarz. 2021. MASTER: FIREX-AQ Airborne Campaign, Western-
693   Central USA, Summer 2019. ORNL DAAC, Oak Ridge, Tennessee, USA.
694   https://doi.org/10.3334/ORNLDAAC/1941

695   Dai, C., Wang, Q., Kalogiros, J.A., Lenschow, D. H., Zhou, M., 2014. Determining Boundary-Layer
696   Height from Aircraft Measurements. Boundary Layer Meteorol. 152, 277–302,
697   https://doi.org/10.1007/s10546-014-9929-z

698   Day, B. M., Rappenglück, B., Clements, C.B., Tucker, S. C., Brewer, A., 2010. Nocturnal boundary layer
699   characteristics and land breeze development in Houston, Texas during TexAQS II. Atmos. Environ.,
700   44(33), 4014–4023. https://doi.org/10.1016/j.atmosenv.2009.01.031.

701   Dreessen, J., Sullivan, J., Delgado, R., 2016. Observations and impacts of transported Canadian wildfire
702   smoke on ozone and aerosol air quality in the Maryland region on June 9–12, 2015, J. Air & Waste
703   Management Assoc., 66:9, 842-862.

704   Finardi, S., Agrillo, G., Baraldi, R., Calori, G., Carlucci, P., Ciccioli, P., D'Allura, A., Gasbarra, D., Gioli,
705   B., Magliulo, V., Radice, P., Toscano, P., Zaldei, A. 2018. Atmospheric Dynamics and Ozone Cycle
706   during Sea Breeze in a Mediterranean Complex Urbanized Coastal Site, Journal of Applied
707   Meteorology and Climatology, 57(5), 1083-1099.

708   Foley, K. M., Roselle, S. J., Appel, K. W., Bhave, P. V., Pleim, J. E., Otte, T. L., Mathur, R., Sarwar, G.,
709   Young, J. O., Gilliam, R. C., Nolte, C. G., Kelly, J. T., Gilliland, A. B., Bash, J. O., 2010.
710   Incremental testing of the Community Multiscale Air Quality (CMAQ) modeling system version 4.7,
711   Geosci. Model Dev., 3, 205-226.

712   Gan, C., Wu, Y., Madhavan, B., Gross, B., Moshary, F., 2011. Application of active optical sensors to
713   probe the vertical structure of the urban boundary layer and assess anomalies in air quality model
714   PM2.5 forecasts, Atmos. Environ., 45 (37), 6613-6621.

715   Griffin, D., Zhao, X., McLinden, C. A., Boersma, F., et al., 2019. High-Resolution Mapping of Nitrogen
716   Dioxide with TROPOMI: First Results and Validation over the Canadian Oil Sands. Geophy. Res.
717   Lett., 46(2): 1049–1060.

718   Haeffelin, M., Angelini, F., Morille, Y., Martucci, G., Frey, S., Gobbi, G.P., Lolli, S., O'Dowd, C.D.,
719   Sauvage, L., Xueref-Remy, I., Wastine, B., Feist, D.G. 2012. Evaluation of mixing-height retrievals
720   from automated profiling lidars and ceilometers in view of future integrated networks in Europe.
721   Boundary-Layer Meteorol. 143, 49–75.

722   Haman, C. L., Couzo, E., Flynn, J. H., Vizuete, W., Heffron, B., Lefer, B. L. 2014. Relationship between
723   boundary layer heights and growth rates with ground-level ozone in Houston, Texas, J. Geophys.
724   Res. Atmos., 119, 6230–6245, doi: 10.1002/2013JD020473.

725   Han, Z. S., González-Cruz, J. E., Liu, H. N., Melecio-Vázquez, D., Gamarro, H., Wu, Y., Moshary, F.,
726   Bornstein, R. 2022. Observed sea breeze life cycle in and around NYC impacts on PBL and surface
727   UHI and ozone patterns, Urban Climate, 42, 101109, doi.org/10.1016/j.uclim.2022.101109

728   Huang, J., J. McQueen, J. Wilczak, I. Djalalova, I. Stajner, P. Shafran, D. Allured, P. Lee, L. Pan, D.
729   Tong, H. Huang, G. DiMego, S. Upadhayay, L. Monache, 2017. Improving NOAA NAQFC PM$_{2.5}$
730   predictions with a bias correction approach, Wea. and Forecasting, 32, 407-421.

731   June, N. A., Hodshire, A. L., Wiggins, E. B., et al., 2022: Aerosol size distribution changes in FIREX-AQ
732   biomass burning plumes: the impact of plume concentration on coagulation and OA
733   condensation/evaporation, Atmos. Chem. Phys., 22, 12803–12825.

734 Karambelas, A., 2020. LISTOS: Toward a Better Understanding of New York City's Ozone Pollution
735   Problem (An overview of the Long Island Sound Tropospheric Ozone Study). EM A&WMA,
736   https://www.awma.org/content.asp?admin=Y&contentid=657
737 Kelly, J. T., Bhave, P. V., Nolte, C. G., Shankar, U., Foley, K. M. 2009. Simulating emission and
738   chemical evolution of coarse sea-salt particles in the Community Multiscale Air Quality (CMAQ)
739   model. Geosci. Model Dev., 2, 1335–1374.
740 Lee, P., J. McQueen, I. Stajner, J. Huang, L. Pan, D. Tong, H. Kim, Y. Tang, Kondragunta S., M.
741   Ruminski, S. Lu, E. Rogers, R. Saylor, P. Shafran, H. Huang, J. Gorline, S. Upadhayay, R. Artz,
742   2017. NAQFC developmental forecast guidance for fine particulate matter (PM2.5). Wea. and
743   Forecasting. 32 (1): 343–360.
744 Li, D., Wu, Y., Gross, B., Moshary, F., 2021. Capabilities of an Automatic Lidar Ceilometer to Retrieve
745   Aerosol Characteristics within the Planetary Boundary Layer. Remote Sens., 13, 3626.
746   https://doi.org/10.3390/rs13183626
747 Li, D., Wu, Y., Gross, B., Moshary, F., 2022. Dynamics of Mixing Layer Height and Homogeneity from
748   Ceilometer-Measured Aerosol Profiles and Correlation to Ground Level PM2.5 in New York City.
749   Remote Sens. 14, 6370. https://doi.org/10.3390/rs14246370
750 Liu, T., Panday, F.M., Caine, M.C., Kelp, M., Pendergrass, D.C., Mickley, L., 2023. Is the smoke aloft?
751   Caveats regarding the use of the Hazard Mapping System (HMS) smoke product as a proxy for
752   surface smoke presence across the United States. Int. J Wildland Fire,
753   https://doi.org/10.31223/X51963
754 Miller, P. J., 2017. Retrospective and Future Analysis of Air Quality In and Downwind of New York
755   City, DRAFT White Paper, available at www.nescaum.org/documents/listos.
756 Ren, X., Salmon, O. E., Hansford, J. R., et al., 2018. Methane Emissions from the Baltimore-Washington
757   Area Based on Airborne Observations: Comparison to Emissions Inventories, J. Geophys. Res.
758   (Atmos.), 123, 8869–8882.
759 Ren, X., Hall, D. L., Vinciguerra, T., Benish, S. E., Stratton, P. R., et al., 2019. Methane emissions from
760   the Marcellus Shale in southwestern Pennsylvania and northern West Virginia Based on Airborne
761   Measurements, J. Geophys. Res. Atmos., 124, 1862–1878.
762 Ring, A., Dickerson, R. R., Sebol, A., Ren, X., Benish, S., Salawitch, R., Galasyn, A., Miller, P., Canty,
763   T., 2023. Anthropogenic VOCs in the Long Island Sound, NY Airshed and their role in ozone
764   production, Atmos. Environ., 296, 119583, https://doi.org/10.1016/j.atmosenv.2023.119583.
765 Ruminski, M., Kondragunta, S., Draxler, R., Zeng, J., 2006. Recent Changes to the Hazard Mapping
766   System, 15th International Emission Inventory Conference, Reinventing Inventories - New Ideas in
767   New Orleans, New Orleans, May 15 - 18, 2006.
768 Schween, J. H., Hirsikko, A., Lohnert, U., Crewell, S., 2014. Mixing-layer height retrieval with
769   ceilometer and Doppler lidar from case studies to long-term assessment. Atmos. Meas. Tech. 7,
770   3685–3704.
771 Seidel, D. J., Ao, C. O., Li, K. 2010. Estimating climatological planetary boundary layer heights from
772   radiosonde observations: Comparison of methods and uncertainty analysis, J. Geophys. Res., 115,
773   D16113, doi: 10.1029/2009JD013680.
774 Shrestha, B., Brotzge, J. A., Wang, J., Bain, N., Thorncroft, C. D., Joseph, E., Freedman, J., Perez, S.
775   2021. Overview and Applications of the New York State Mesonet Profiler Network, J. Appl.
776   Meteorol. Climat. https://journals.ametsoc.org/view/journals/apme/aop/JAMC-D-21-0104.1/JAMC-
777   D-21-0104.1.xml
778 Stauffer, R. M., Thompson, A. M., Martins, D. K., Clark, R. D., Goldberg, D. L., Loughner, C. P.,
779   Delgado, R., Dickerson, R. R., Stehr, J. W., Tzortziou, M. A., 2015. Bay breeze influence on surface
780   ozone at Edgewood, MD during July 2011. J. Atmos. Chem., 72(3-4), 335–353.

781 Stein, A., Draxler, R., Rolph, G., Stunder, B., Cohen, M., Ngan, F. 2015. NOAA's HYSPLIT atmospheric
782   transport and dispersion modeling system. Bulletin of the American Meteorological Society. 96 (12)
783   2059-2077. doi: 10.1175/BAMS-D-14- 00110.1.
784 Stull, R.B., 1988. An Introduction to Boundary Layer Meteorology. Kluwer Academic Publishers, pp.
785   12–16.
786 Sullivan, J. T., Berkoff, T., Gronoff, G., Knepp, T., et al. 2019. The Ozone Water–Land Environmental
787   Transition Study: An Innovative Strategy for Understanding Chesapeake Bay Pollution Events,
788   Bulletin of the American Meteorological Society, 100(2), 291-306.
789 Tao, Madankui, Arlene M. Fiore, Xiaomeng Jin, Luke D. Schiferl, Róisín Commane, Laura M. Judd,
790   Scott Janz, John T. Sullivan, Paul J. Miller, Alexandra Karambelas, Sharon Davis, Maria Tzortziou,
791   Lukas Valin, Andrew Whitehill, Kevin Civerolo, Yuhong Tian, 2022. Investigating Changes in
792   Ozone Formation Chemistry during Summertime Pollution Events over the Northeastern United
793   States, Environ. Sci. Technol., 56 (22), 15312-15327, DOI: 10.1021/acs.est.2c02972
794 Torres-Vazquez, A., Pleim, J., Gilliam, R., Pouliot, G., 2022. Performance Evaluation of the Meteorology
795   and Air Quality Conditions from Multiscale WRF-CMAQ Simulations for the Long Island Sound
796   Tropospheric Ozone Study (LISTOS). J. Geophy. Res.: Atmospheres, 127(5):e2021JD035890,
797   https://doi.org/10.1029/2021JD035890.
798 Tucker, S.C., Senff, C.J., Weickmann, A.M., Brewer, W.A., Banta, R.M., Berg, S.P., Law, D. C.,
799   Hardesty, R.M., 2009. Doppler idar estimation of mixing height using turbulence, shear, and aerosol
800   profiles. J. Atmos. Ocean. Technol. 26, 673–688.
801 Taubman, B. F., Marufu, L. T., Piety, C. A., Doddridge, B. G., Stehr, J. W., Dickerson, R. R. 2004.
802   Airborne characterization of the chemical, optical, and meteorological properties, and origins of a
803   combined ozone-haze episode over the eastern United States, J. Atmos. Sci., 61, 1781-1793.
804 Vermeuel, M. P., Novak, G. A., Alwe, H. D., Hughes, D. D., et al., 2019. Sensitivity of ozone production
805   to NOx and VOC along the Lake Michigan coastline. J. Geophys. Res. (Atmos.), 124 (20), 10989-
806   11006.
807 Winker, D. M., M. A. Vaughan, A. Omar, Y. Hu, and K. A. Powell, Z. Liu W. H. Hunt, S. A. Young, 2009.
808   Overview of the CALIPSO Mission and CALIOP Data Processing Algorithms, J. Atmos. Oceanic
809   Technol., 26, 2310–2323.
810 Wu, Y., Chaw, S., Gross, B., Moshary, F., Ahmed, S., 2009. Low and optically thin cloud measurements
811   using a Raman-Mie lidar, Appl. Opt. 48, 1218-1227.
812 Wu, Y., L. Cordero, B. Gross, Moshary, F., Ahmed, S. 2012. Smoke plume optical properties and
813   transport observed by a multi-wavelength lidar, sunphotometer and satellite, Atmos. Environ., 63,
814   32–42.
815 Wu, Y., Zhao, K., Huang, J., Arend, M., Gross, B., Moshary, F. 2019. Observation of heat wave effects
816   on the urban air quality and PBL in New York City area, Atmos. Environ, 117024, DOI:
817   10.1016/j.atmosenv.2019.117024.
818 Wu, Y., Nehrir, A., Ren, X., Dickerson, R. R., Huang, J., et al., 2021. Synergistic aircraft and ground
819   observations of transported wildfire smoke and its impact on air quality in New York City during the
820   summer 2018. Sci. Total Environment. 773, 145030. https://doi.org/10.1016/j.scitotenv.2021.145030
821 Zhang, J., Ninneman, M., Joseph, E., Schwab, M. J., Shrestha, B., Schwab, J. J. 2020. Mobile laboratory
822   measurements of high surface ozone levels and spatial heterogeneity during LISTOS 2018: evidence
823   for sea breeze influence. J. Geophys. Res. (Atmos.) 125 (11), 1–19.Zhang, D., Comstock, J., Morris,
824   V. 2022. Comparison of planetary boundary layer height from ceilometer with ARM radiosonde
825   data, Atmos. Meas. Tech., 15, 4735–4749, https://doi.org/10.5194/amt-15-4735-2022.
826 Zhao, K., Bao, Y., Huang, J., Wu, Y., Arend, M., Moshary, F., 2019. A high-resolution modeling study of
827   a heat wave-driven ozone exceedance event in New York City and surrounding regions, Atmos.
828   Environ., 199, 368–379.

829   Zhao, K., Wu, Y., Huang, J., Gronoff, G., Berkoff, T., Arend, M., Moshary, F., 2023. Identification of the
830   roles of urban plume and local chemical production in ozone episodes observed in Long Island
831   Sound during LISTOS 2018: implications for ozone control strategies, Environment International,
832   174, 107887, https://doi.org/10.1016/j.envint.2023.107887.
833
834

Figures and Table Captions

Table-1. Ground site location and the data used in this study.

Table-2. PBLH comparison among the methods from ceilometer, wind lidar and virtual potential temperature (θ_v) at the North-shore of Long Island (UTC-4=local time or EDT)

Fig.1. Ground sites used in this study (See Table-1 for their coordinates and observations).

Fig. 2. Temporal variation of (a) near-surface O_3 and (b) NO_2 in the NYC urban and coastal area in Long Island during July 25-31, 2019; (c)-(d) Daily O_3-AQI on July 28 and 29, 2019 from AirNow. FP-Flax Pond, QC-Queens College, see Fig.1 and Table-1 for the site full names and locations.

Fig. 3. (a)-(b) Air temperature and RH at CCNY (1-min ave.), Stony Brook (SBK in NLI) and Fire Island (FI in SLI), (c) Wind rose at 6:00-18:00 EDT on July 25-26 and (d) July 28-30 at CCNY.

Fig.4. Comparison of MLH measured from the methods of (a) Ceilometer, (b) Wind lidar, (c–f) Virtual potential temperature (θ_v) and water vapor (H_2O) profiles at the North-shore of Long Island on July 29, 2019. (Vertical dash lines in Fig. (a): ozonesonde launch time; horizontal dash lines in (c-f): PBLH)

Fig.5. Vertical profiles of (a) aerosol total scattering coefficient (σ_{as}) at λ=550-nm, (b) virtual potential temperature (θ_v), and (c) water vapor (H_2O) measured from the UMD research aircraft near Flax Pond at 19:32-19:52 UTC on July 29, 2019. (Horizontal dash lines – PBLH estimate from each method)

Fig. 6. Ceilometer-measured backscatter intensity and MLH at (a) CCNY, (b) Eatons Neck, and (c) Fire Island during July 26-31, 2019. (MLH:mixing-layer-height; Cldz:cloud base; ALH: aerosol-layer-height)

Fig. 7. Comparison and correlation of MLH (30-min ave.) between the ceilometer and wind-lidar methods in the NYC urban (a-b), and the NLI coastal area (c-d), respectively.

Fig. 8. Diurnal variation of ground O_3 (a), MLH (b), and (c) Ratio of vertical velocity variance from the wind lidar measurements in the NYC urban and the coastal area in North-shore of Long Island (NLH) on July 28-30, 2019 (red circles: MLH in the urban area).

Fig.9. (a) Wind lidar measured carrier-noise-ratio (CNR), (b) horizontal wind speed, (c) wind direction, (d) vertical wind velocity (+up, –down) at Bronx (NYC urban) during July 28-31, 2019.

Fig.10. Same as Fig.9 except at Stony Brook (SBK) in the Northern Long Island.

Fig.11. (a) Vertical distribution of O_3, (b) wind speed (Spd) and direction (Dir.) measured from the ozonesonde at Flax Pond at 14:29-14:40 UTC on July 29, 2019 (vertical dash: wind direction at 270º).

Fig. 12. (a)-(b) Same as Fig.11 except at 19:14-19:22 UTC on July 29, 2019 (afternoon).

Fig.13. (a) Aircraft flight track and time-height for the two vertical profile measurements (P1- ascent in green; P2- descent in red), (b)-(g) Profiles of O_3, CO, aerosol scattering coefficient (horizontal dash-PBLH), NO_x, CH_4, HCHO on July 29, 2019. P1: 19:32-19:52UTC near Flax Pond; P2: 19:52-20:15UTC cross LIS.

Fig.14. (a)-(d). Tropospheric column content of NO_2 and HCHO measured from S5P/TROPOMI/ on July 28 (a, b) and 30 (c, d), 2019

Fig.15 (a)-(b) Comparisons of ground-level hourly O_3 between the WRF-Chem, NAM-CMAQ model and the observations, (c) MLH comparison in the coastal area of Long Island during July 28-30, 2019.